Modeling of Flow in Impeller Stirred Tanks using Computational Fluids Dynamics

By

Namwawa Alice Siwale

B.Sc. Mechanical Engineering (University of Cape Town)

A Thesis submitted in part fulfillment of the requirements for the degree of Masters in Engineering

Department of Mechanical Engineering

University of Cape Town

August 2004

Acknowledgements

I would like to express my sincere thanks to the following people:

My supervisor Dr Chris Meyer my and co-supervisor Dr David Deglon for their guidance

My parents, Peart and Nancy Siwale for their emotional and financial support

My siblings and friends Zewe, Chiluwa, Tontela, Mengo and Christopher Malabie for their constant encouragement

Last but not least, I would like to thank my Lord Jesus Christ through whom all things have been made possible.

Plagiarism Declaration

I know the meaning of plagiarism and hereby declare that the work in this document, save for that which is properly acknowledged is my own.

Signed…….. Date……..

Namwawa Alice Siwale.

TABLE OF CONTENTS

LIST OF FIGURES

LIST OF TABLES

LIST OF APPENDICES

NOMENCLATURE

a	Impeller blade width (m)
b	Impeller hub diameter (m)
B	Constant which is a function of wall roughness (dimensionless)
C	Off bottom impeller clearance (m)
C_μ $C_{1\varepsilon}$ $C_{2\varepsilon}$	Empirical coefficients in turbulent transport equation
d	Impeller disc diameter (m)
D	Impeller diameter (m)
F_i	Fluid variable source term in transport equation
Fr	Froude number, $(N^2D)/g$ (dimensionless)
g_i	Body force due to gravity (N)
G_k	Generation of turbulent kinetic energy (s^{-1})
h	Impeller blade height (m)
H	Height of fluid in the tank (m)
k	Turbulent kinetic energy (m^2/s^{-2})
N	Impeller speed (s^{-1}).
$\overline{n}$	Normal unit vector (m)
n_p	Normal distance from wall (m)
N_p	Impeller power number, $P/(\rho N^3 D^5)$ (dimensionless)
N_Q	Impeller pumping number, $Q/(ND^3)$ (dimensionless)
r	Radial coordinate distance (m)
Pe	Cell Peclet number (dimensionless)
Re	Reynolds number $(\rho ND^2)/\mu$ (dimensionless)
t	Time (s)
T	Tank diameter (m)
u_i	General velocity component (m/s)
u_i'	Turbulent fluctuating velocity component (m/s)
$\overline{u}_i$	Time-averaged velocity component (m/s)
u, v, w	Velocities in the three coordinate components (m/s)
U^+	Non-dimensional wall parallel velocity (dimensionless)
U_{tip}	Impeller tip velocity (m/s)
w	Baffle width (m)

x_i	Cartesian space coordinate (m)
y^+	Non-dimensional coordinate normal to wall
z	Vertical coordinate direction (m)

Greek Letters

ε	Rate of dissipation of turbulence energy (m^2/s^3)
ε_{ijk}	Cyclic permutation symbol
κ	Von Kármán constant
ρ	Density (kg/m^3)
$\sigma_\varepsilon,\sigma_k$	Effective turbulent Prandtl numbers for the transport of ε and k.
δ_{ij}	Kroenecker delta.
τ_w	Wall shear stress (Nm^{-1})
μ	Dynamic viscosity (kg/ms)
μ_t	Effective turbulent viscosity (kg/ms)
ω	Rotational speed (^-s)
ϕ	Generalized dependent flow variable
θ	Circumferential coordinate direction (radians)

Subscripts

e	Value at right face of cell
i, j, k	Subscripts denoting Cartesian coordinate directions
E, P, W	Values at nodes to the right, center and left
tip	Values at impeller blade tip

Superscripts

+	Denotes quantity non-dimensionalized by μ, τ_w and ρ.

Abbreviations

CD	Central differencing
IBC	Impeller boundary conditions
LDV	Laser Doppler Velocimetry
MRF	Multiple Reference Frames

PIV	Particle Image Velocimetry
RMS	Root-mean-square
RSM	Reynolds Stress Model
SM	Sliding Mesh
UD	Upwind differencing

ABSTRACT

The efficiency of mixing processes in impeller agitated tanks depends highly on the hydrodynamics. Computational fluids dynamics (CFD) provides a method of predicting the complex flow structures in stirred tanks. As with any approximate numerical method, CFD methods are subject to errors due to assumptions in the underlying mathematical models, as well as errors due to the numerical solution procedures.The aim of this thesis was to present a CFD method that accurately models the hydrodynamic properties of the flow in stirred tanks.

The general purpose CFD software *Fluent 6.1* was used to develop the model of a laboratory-scale stirred tank. Numerical experiments were conducted to investigate the effects of the computational grid density, discretization schemes, turbulence models and impeller modeling method on the accuracy of the simulated flow. The results were validated with Laser Doppler Velocimetry data from the literature.

It was found that the density of the numerical grid had more influence on the predicted turbulent quantities than on the mean velocity components. For the mean velocity components, reasonable agreement with the experimental data was observed even on relatively coarse grids. The choice of discretization scheme was found to have significant effect on the predicted turbulent kinetic energy and Power numbers. Very good agreement with experimental data was achieved for both these flow variables when higher order discretization schemes were used on fine grids. This is an important finding as it suggests that the generally reported underestimation of turbulence in literature is caused by numerical errors in the CFD simulation as opposed to inadequacies in the turbulence models as suggested by most researchers.

Steady-state and time-dependent impeller models were compared and found to have little effect on the mean velocity and turbulent kinetic energy. However impeller Power numbers calculated from the time-dependent simulations were found to be in better agreement with the experimental values. A comparison was also made between the standard k-ε and RNG models. It was found that the standard k-ε turbulence model gave better predictions of the flow than the RNG- k-ε turbulence model.

CHAPTER 1 INTRODUCTION

1.1. Overview

In engineering practice, impeller stirred tanks are used for a wide variety of mixing operations involving both single liquid phase and multi-phase processes. In the mineral processing industry for example, impeller stirred tanks are used for solid particle suspension and gas dispersion in the flotation process. As efficient mixing is critical to these processes, considerable effort has been devoted to the detailed understanding of the fluid dynamics in stirred tanks.

The six-bladed disc or Rushton turbine impeller has received the most attention because of its widely accepted application in processes involving low viscosity fluids that often occur in industry. Over the years, a standard vessel configuration with vertical baffles along the tank periphery has evolved (Figure 1-1). The baffles prevent the formation of a central vortex and minimize solid body rotation of the fluid, a situation that is detrimental to mixing. This standard configuration is based on power draw studies and should be viewed as a point of reference for improved stirred vessel design (Tatterson, 1991).

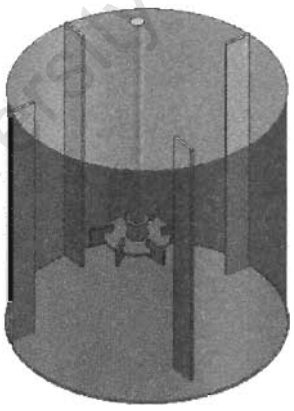

Figure 1-1: Standard baffled stirred tank configuration with Rushton turbine impeller.

1.2. Hydrodynamic Properties of Stirred Tanks

The flow structures in a stirred tank depend on a number of parameters, including the shape and size of the impeller, geometric configuration of the tank and operating conditions such as

impeller rotational speed. Flow properties such as velocity, turbulent kinetic energy and turbulent energy dissipation rates can be used to characterize the flow throughout the vessel. It is therefore desirable to relate the required performance characteristics of the stirred tank to these fluid dynamic properties, in order to make appropriate choices in hardware and operating conditions.

Velocity distributions give an insight into the flow patterns generated in the stirred tank and in identifying regions of rich and poor mixing. This in turn assists in selecting suitable impellers for particular applications. For example, in solid suspension applications, an impeller that generates an axial flow pattern is desired in order to sweep the solids off the bottom of the tank. Higher-level parameters such as vorticity, shear rates and elongation, which are critical in processes such as polymerization (Fields and Ottino, 1987), fermentation and cell culture engineering (Converti et al., 1996), are also derived from velocity distributions. In most studies of engineering relevance, a detailed description of all turbulent quantities in the stirred tank is not necessary and a statistical approach is usually employed. This involves resolving the flow variables into mean values and small scale fluctuating components. Apart from the mean and root-mean-square fluctuating velocities, two quantities that are important in mixing studies are the turbulent kinetic energy, k and the turbulent energy dissipation rate ε.

Turbulent energy dissipation rate is incorporated into many reactor engineering models. For example in mineral flotation studies, ε is incorporated into bubble break-up and coalescence models (Bakker, 1992; Deglon, 1998; Lane et al., 2002), and in chemical reacting processes, ε is incorporated in micro-mixing models for determining blending time and product distribution (Ranade and Van Den Akker, 1994). Therefore, understanding how ε is distributed in the stirred vessel and how this distribution is affected by design and operating conditions like scale-up, operating speed of impeller, etc., is necessary. Values of the turbulent kinetic energy k in the stirred vessel can be obtained from measurements of the fluctuating velocities (RMS values) and the energy dissipation rates calculated from k using turbulence macro scale models (Wu et al., 1989a-b; Lee and Yianneskis, 1998). As might be expected, the highest values of energy dissipation are found in the high speed regions around the impeller blades and in the impeller discharge stream. Therefore most studies of turbulence in stirred tanks focus on this region.

Various parameters have been defined to quantify the performance characteristics of impellers in stirred tanks. These values, based on dimensional analysis, are used as a basis for the selection of suitable impellers and as guidance in the scale-up of mixing processes (Wernerson and Tragardh,

1999). The performance of an impeller is dependent on geometric factors such as the ratios of impeller diameter to tank diameter (D/T), impeller clearance to tank diameter (C/T), and also the operating speed of the impeller. Important parameters for the design and scale-up of stirred tanks include the Power number N_P, the Pumping number N_Q and mixing time N_θ.

1.3. Methods of Measuring Fluid Flow Variables

The complexity of the flow in stirred vessels, and indeed many other practical flow problems, prevents the sound application of analytical studies. Hence up to recent years, most developments in fluid flow equipment have been based on empirical studies. Mavros (2001) has presented a comprehensive review of the different flow measuring techniques in stirred tanks. In earlier studies, simple techniques like pitot-tubes were used to quantify the velocity fields in stirred tanks. Later, hot wire anemometry was introduced and has also been used to measure flow variables in stirred tanks, especially gas-liquid flows. The main disadvantage with the Pitot tube and hot wire techniques is that they are intrusive and may affect the flow being measured.
In recent studies, detailed measurements of flow in stirred vessels have been obtained using non-intrusive techniques such as laser Doppler Velocimetry, LDV (Yianneskis et al., 1987; Wu and Patterson, 1989a; Morud and Hjertager, 1996) or Particle Image Velocimetry, PIV (Dyster et al., 1993; Mavros et al., 1996; Schafer et al., 1997; Lee and Yianneskis, 1998; Aubin et al., 2004b). Although these advanced methods have been shown to give detailed information on the flow fields in stirred tanks, they are often impractical for industrial applications. These experimental methods require for example, that the fluid and the vessel are transparent in order to allow laser light transmission. In the case of gas-liquid flow, gas quantities are restricted to small amounts in order to avoid light scattering in LDV and bubble interference in PIV images (Aubin et al., 2004b). However, most often in industry, the fluid is opaque and the vessels are made from non-transparent materials and in gas-liquid flows, the required gassing rates are high. Also, high quality experimental facilities using LDV or PIV are relatively expensive.

In view of the complex nature of the flow in stirred tanks that precludes analytical solution and the limitations of experimental methods outlined above, a considerable amount of effort has been devoted towards the numerical prediction of the flow. Recent advances in the development of efficient numerical solution procedures, coupled with the immense increase in computational power, have promoted the research into the use of Computational Fluids Dynamics (CFD) as a reliable tool in design of fluid flow processes. CFD involves the use of digital computers to

predict the flow field in the system of interest by numerical solution of the transport equations of flow variables such as mass and momentum.

1.4. Scope of Thesis

This thesis was initiated as part of the studies intended to incorporate CFD into the Mineral Flotation research being conducted at the University of Cape Town. It is strongly believed that before CFD can be confidently used in the study of complex multi-phase processes such as those occurring in the flotation process, it is important to examine the accuracy of the technique in simulating less complex single phase flows in stirred tanks. Therefore, in the present study, the accuracy of CFD techniques in predicting the flow of single phase fluids in stirred tanks was investigated, with the vision of extending this study to multi-phase flows involving gases and solids.

A critical analysis of many publications concerning the numerical simulation of fluid flow in baffled impeller agitated tanks shows several discrepancies. The most important differences concern the modeling approaches for the rotation of the impeller, turbulence modeling, as well as the accuracy of the numerical predictions.
In any numerical calculation, there are two sources of errors:

- Error due to the assumptions made on the physical behavior of the system. In the stirred tank case, this pertains to assumptions made in deriving the mathematical models of the mixing process, turbulence models and the method of modeling the rotation of the impeller.
- Numerical errors, due to the numerical solution procedures, such as inadequate grids and discretization practices for the underlying equations of the mathematical models.

Most studies have concentrated on the assessment of the various mixing process models, turbulence models and on the method used to specify the rotating impeller, with not as much effort given to the numerical solution procedure. However, in order that solutions purely reflect the outcome of the various physical models, it is necessary to isolate as much as possible from the computations any errors due to the numerical solution procedure. The aim of this thesis was to present a CFD method that accurately models the hydrodynamic properties of the flow in stirred tanks. The influence of grid density and discretization schemes on the predicted flow field was

investigated. Two commonly used impeller modeling methods and different turbulence models were also examined.

CHAPTER 2 LITERATURE REVIEW

In this Chapter, the differential equations that govern the flow of a single phase fluid are presented. For the stirred tank system, analytical solution of the governing equations is not possible and the equations need to be solved using numerical methods. The steps involved in the finite volume solution method - grid generation, discretization of the model equations, are described in detailed. This is followed by a review of other studies that have been conducted on CFD modeling of flow in stirred tanks.

2.1. Governing Equations of Fluid Flow

With the assumption of isothermal conditions, the equations governing single phase fluid flow in a stirred tank are the transport equations for mass and momentum. For an incompressible fluid, the transport equation for mass (continuity equation) is written as follows.

$$\frac{\partial u_i}{\partial x_i} = 0 \qquad [2\text{-}1]$$

The transport equations for momentum, known as the Navier-Stokes equations are represented by the following equation.

$$\frac{\partial}{\partial t}(\rho u_i) + \frac{\partial}{\partial x_j}(\rho u_i u_j) = -\frac{\partial p}{\partial x_i} + \frac{\partial}{\partial x_j}\left(\mu\left(\frac{\partial u_j}{\partial x_i} + \frac{\partial u_i}{\partial x_j}\right)\right) + \rho g_i + F_i \qquad [2\text{-}2]$$

The equations presented above need to be solved in order to obtain values of the velocity components, turbulent kinetic energy and turbulent energy dissipation rates in the isothermal incompressible system of interest.

2. 2. Turbulence Modeling

The equations outlined in the previous section are applicable to both laminar and turbulent flows and thus in principle can be calculated directly using numerical methods for both these flow regimes. Turbulent flows are however characterized by variables that are randomly fluctuating in

three dimensions and these fluctuations can be of very small scale and high frequency. Direct solution of turbulent flows using numerical methods would therefore require grids with an immense and often impractical number of grid points in order to resolve these small scales and high frequencies.

2.2.1. Time Averaging

As mentioned in Chapter 1, for studies of flows that are of practical engineering relevance, detailed description of turbulence is not necessary. The governing equations are instead time-averaged, resulting in a modified set of equations that are less demanding to solve. In a randomly unsteady turbulent flow, time-averaging can be used to resolve any variable into an average and fluctuating component. The instantaneous velocity, for example, becomes:

$$u_i = \overline{u}_i + u_i' \qquad [2\text{-}3]$$

Where, the mean value is given by the following time average.

$$\overline{u}_i = \frac{1}{T}\int_{t_0}^{t_0+T} u_i\,dt \qquad [2\text{-}4]$$

The time T, over which the mean is taken is large compared to the period of fluctuation of u_i and thus small details of the flow are lost. Each dependent variable in the transport equation is substituted by its mean and fluctuating term and time averaged, resulting in the following modified set of governing equations known as the Reynolds-averaged equations.

Reynolds Averaged Continuity Equation

$$\frac{\partial \overline{u}_i}{\partial x_i} = 0 \qquad [2\text{-}5]$$

Reynolds Averaged Navier-Stokes Equation

$$\frac{\partial}{\partial t}(\rho\overline{u}_i) + \frac{\partial}{\partial x_j}\left(\rho\overline{u}_j\overline{u}_i + \rho\overline{u_j'u_i'}\right) = -\frac{\partial \overline{p}}{\partial x_j} + \frac{\partial}{\partial x_j}\left(\mu\left(\frac{\partial \overline{u}_j}{\partial x_i} + \frac{\partial \overline{u}_i}{\partial x_j}\right)\right) + \rho g_i + \overline{F}_i \qquad [2\text{-}6]$$

Time averaging introduces six unknown terms represented by the tensor $\rho\overline{u_j' u_i'}$ and referred to as the Reynolds stresses. For closure of the governing transport equations, it is necessary to relate these Reynolds stresses to known or calculable quantities. This is done through various turbulence models.

2.2.2. The k-ε Turbulence Model

Experimental observation has shown that for isothermal incompressible flows, the Reynolds stresses are proportional to the mean velocity gradient. Using Boussinesq's hypothesis of a turbulent eddy viscosity, μ_t (White, 1991), the following relation between the Reynolds stresses and the mean velocity gradients was formulated.

$$-\rho\overline{u_i' u_j'} = \mu_t\left(\frac{\partial \bar{u}_j}{\partial x_i} + \frac{\partial \bar{u}_i}{\partial x_j}\right) - \frac{2}{3}\rho\delta_{ij}k \qquad [2\text{-}7]$$

In the above equation, the turbulent kinetic energy k is defined by the following relation.

$$k \equiv \frac{1}{2}\overline{u_i' u_i'} \qquad [2\text{-}8]$$

In the k-ε turbulence model, the following empirical relation is used to calculate the turbulent viscosity.

$$\mu_t \approx C_\mu \rho \frac{k^2}{\varepsilon} \qquad [2\text{-}9]$$

Values of k and ε are needed to close the set of model equations. These values are determined from their respective transport equations as follows:

Turbulent Kinetic Energy:

$$\frac{\partial}{\partial t}(\rho k)+\frac{\partial}{\partial x_i}(\rho u_i k)=\frac{\partial}{\partial x_i}\left(\left(\mu+\frac{\mu_t}{\sigma_k}\right)\frac{\partial k}{\partial x_i}\right)+G_K-\rho\varepsilon \qquad [2\text{-}10]$$

Turbulent Energy Dissipation Rate:

$$\frac{\partial}{\partial t}(\rho \varepsilon)+\frac{\partial}{\partial x_i}(\rho u_i \varepsilon)=\frac{\partial}{\partial x_i}\left(\left(\mu+\frac{\mu_t}{\sigma_\varepsilon}\right)\frac{\partial \varepsilon}{\partial x_i}\right)+\frac{\varepsilon}{k}C_{\varepsilon 1}G_K-C_{\varepsilon 2}\rho\frac{\varepsilon^2}{k} \qquad [2\text{-}11]$$

G_k represents a generation term for turbulent kinetic energy.

$$G_k=\mu_t\left(\frac{\partial u_i}{\partial x_j}+\frac{\partial u_j}{\partial x_i}\right)\frac{\partial u_j}{\partial x_i} \qquad [2\text{-}12]$$

The constants in the model relations are obtained from empirical correlations. For the standard k-ε model, Lauder and Spalding (1974) proposed the following dimensionless constants after extensive examination of free turbulent flows:

$$C_\mu=0.09 \qquad \sigma_k=1.0 \quad \sigma_\varepsilon=1.3 \quad C_{\varepsilon 1}=1.44 \quad C_{\varepsilon 2}=1.92$$

Although the standard form of the k- ε model has been used successfully for a wide range of flow problems, certain limitations have been observed. The model has been known to perform poorly in highly swirling flows with strong streamline curvature and vortex generation (Abujelala, 1984; White, 1991; Jenne and Reuss, 1999; Jaworski and Zakrzewska, 2002). Modified forms of the standard k-ε model have been formulated to better represent the flow in such cases. Two commonly used modifications of the standard form are the Chen-Kim and the Renormalized Group (RNG) variants of the k-ε model (Jenne and Reuss, 1999; Montante et al., 2001; Jaworski and Zakrzewska, 2002; Aubin et al., 2004). These variants differ from the standard form in the definition of the transport equation for ε and also in the values of the model constants. The effect of the changes in the Chen-Kim model is to reduce the turbulent viscosity in regions of high shear. Hence, for re-circulating flow involving rapid changes in production of turbulent kinetic

energy and in turbulence dissipation rates, the Chen-Kim modified k-ε model is expected to give better results than the standard form. In the RNG k-ε model, the modifications provide a more accurate description of how the effective turbulent transport varies with the eddy scale, allowing the model to better predict low Reynolds number and near wall flow (*Fluent 6.1* User's Guide (2003)). Most researchers however, have used the standard form of the k-ε model to model the turbulence in stirred tanks, although it is known that this form may fail in flows with strong streamline curvature and vortex generation. Also, since the concept of an eddy viscosity assumes isotropic turbulence, flows driven by anisotropic Reynolds stresses can be poorly predicted by the k- ε models.

2.2.3. Non-isotropic Turbulence Models

Other approaches to turbulence modeling that do not make use of the turbulent eddy viscosity assumption have been formulated. In the Reynolds stress model (RSM), transport equations for each of the six Reynolds stresses are solved, along with the transport of ε. Therefore, the effects of turbulence are represented with greater accuracy in the time-averaged momentum equations and this model is expected to give better predictions than k-ε models for complex three dimensional flows. Since seven additional transport equations are required, the RSM is more computationally intensive than k-ε models and is usually only considered as an alternative when the flow features of interest are the result of high anisotropy in the Reynolds stresses. Theoretically, it is possible to resolve the whole spectrum of turbulent scales by direct solution of the Navier-Stokes equations. However, the range of scales of the turbulent eddies involved in engineering problems makes this approach impractical. In Large eddy simulation (LES) methods, the large eddies are resolved directly, while the small eddies are modeled. LES models are three dimensional and time-dependent but require less restrictive numerical grids than direct solution. However, LES methods are still much more computationally intensive than turbulence models that are based on Reynolds-averaged equations.

2.2.4. Treatment of Flow near Walls

In bounded turbulent flows such as mixing in stirred tanks, there is a thin layer near the wall in which viscous effects are more important than the high inertia effects of the free turbulent flow. Therefore the flow behavior and turbulence structure near the wall are considerably different

from the free flows. For successful prediction of wall-bounded turbulent flows, accurate representation of the near wall flow is necessary (Ranade et al., 1989; Gosman et al., 1992; Bartels et al., 2002).

There are two methods of modeling the flow near solid walls. In one approach, the turbulence models are modified so that they are applicable to the viscous near-wall flow. In the other approach, semi-empirical formulas called *wall functions* are used to bridge this viscous region near the wall and the fully turbulent free flow. The latter is a more practical approach for the study of stirred tanks in which the detailed description of the viscous boundary layer is not necessary. In the standard wall function approach proposed by Lauder and Spalding (1974), the mean velocity profile near the wall is assumed to be of the following form:

$$U^+ = \frac{1}{\kappa}\ln y^+ + B \qquad [2\text{-}13]$$

where κ is the von Kármánn constant, B is an empirical constant related to the viscous layer and U^+ and y^+ are the resultant velocity parallel to the wall and normal wall distance, non-dimensionalized by the wall shear stress, τ_w , density ρ and viscosity, μ. This formula is valid in the near-wall region $30 \le y^+ \le 300$.

The derivation of the wall functions assumes equilibrium between the production of turbulent kinetic energy G_k, and its dissipation rate ε. Turbulent kinetic energy in the near- wall region is obtained as for the rest of the flow in the domain by solving the transport equation of k. However, by assuming local equilibrium, the turbulent energy dissipation rate in the near wall region is computed from an empirical relation:

$$\varepsilon = \frac{C_\mu^{\frac{3}{4}} k^{\frac{3}{2}}}{\kappa n_P} \qquad [2\text{-}14]$$

A detailed description of the wall functions, associated derivations and discussion on limitations can be found in Lauder and Spalding (1974).

2.3. Numerical Solution: Finite Volume Method

2.3.1. Computational Grid

The finite volume numerical solution method starts with the discretization or division of the flow domain into a finite number of control volumes or cells. Nodal positions at which the dependent flow variables are to be calculated are defined within these control volumes, usually centered within the volume. Basically, there are two types of grids: structured and unstructured (c.f. Figure 2-1).

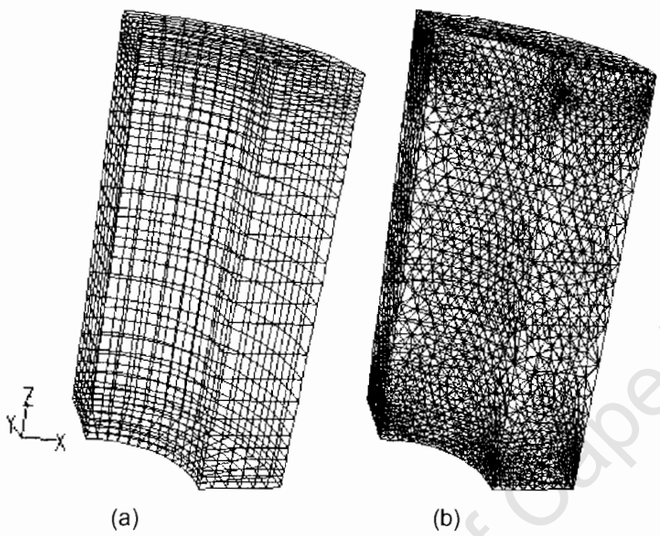

Figure 2.1: Volume discretization with (a) structured and (b) unstructured grids.

The cells in structured grids are hexahedral and each cell has a unique address in each direction of the computational space. This allows for global coordinate transformation from the physical to the computational space and nodes can be numbered consecutively, resulting in an ordered data set. Unstructured grids show no ordering of the control volumes and each nodal location and connecting neighbor must be specified explicitly. Unstructured grids usually contain tetrahedral shaped control volumes.

In general, the accuracy of the solution is improved by using grids with more cells. Unfortunately, the cost of the solution in terms of computation time and storage is also proportional to the number of cells in the calculation. Therefore optimal grids are often non-uniform: finer in places

where high gradients of the flow variable are expected and coarser in places with relatively little spatial or temporal change.

Optimization of calculation speed requires a systematic search for the grid with the least number of cells that will produce a grid-independent solution. This is achieved by carrying out calculations on a series of successively refined grids, until no notable difference in important flow variables is observed. In practice, limitations in computer storage restrict the amount of grid refinement. Therefore, for a particular grid, the accuracy of the numerical prediction can also be improved by careful selection of the differencing scheme.

2.3.2. Discretization of the Governing Equations

The governing equations are applied to each control volume in the numerical grid to develop discrete equations for the nodal points as described below.
The governing transport equations can be cast into a general conservation form which represents the flow of the dependent variable into and out of a control volume.

$$\frac{\partial(\rho\phi)}{\partial t}+\frac{\partial(\rho u_i\phi)}{\partial x_i}=\frac{\partial}{\partial x_i}\left(\Gamma_\phi\frac{\partial\phi}{\partial x_i}\right)+S_\phi \qquad [2\text{-}15]$$

ϕ represents the dependent flow variable (u, v, w, k or ε), Γ_ϕ is the exchange coefficient for diffusion and S_ϕ the source term encompassing all remaining terms. Discretization involves integration of the equation over each control volume with respect to time and space. The integrated form of the equation contains unknown values of the dependent variable and its normal gradients at control volume faces. These need to be approximated in terms of algebraic functions of the value at the discrete nodal positions where problem variables are to be calculated. For this purpose, a selection of interpolation practices has been formulated.

The various interpolation or discretization schemes must possess certain properties in order to yield solutions that are both physically and numerically realistic. These properties can be demonstrated by discussing the limitations placed on the non-dimensional cell Peclet number *Pe*,

which gives the relative strengths of the convective and diffusive fluxes through the control volume.

$$Pe = \frac{\rho u_x \Delta x}{\Gamma} \qquad [2\text{-}16]$$

where Δx represents a characteristic length of the control volume. Some commonly used discretization schemes will be discussed briefly below along with the limitations placed on the cell Peclet number.

2.3.2.1. Central Differencing (CD)

Central Differencing (CD) assumes that quantities vary linearly between two nearest nodal positions so that the value at the common cell face is approximated by linear interpolation. For an arbitrary control volume, such as that illustrated in Figure 2-2, the value of the transported property ϕ at the right hand face is given by the following equation

$$\phi_e = \phi_E \left(\frac{x_e - x_p}{x_E - x_p} \right) + \phi_p \left(1 - \frac{x_e - x_p}{x_E - x_p} \right) \qquad [2\text{-}17]$$

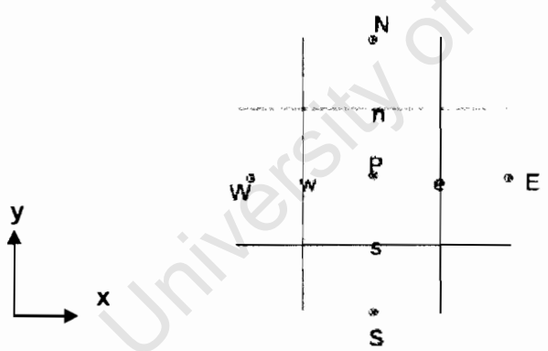

Figure 2-2: Arbitrary control volume in 2D (W, P, E, N, and S represent nodal positions).

From a Taylor series expansion, it can be shown that the CD scheme possesses second-order accuracy (Ferziger, 1997). Similar expressions are derived for values at the other cell faces. To formulate and expressions for all the faces of the control volume, values at all adjacent nodal

positions are required. Thus in CD, the value of the dependent variable at a particular nodal position, for example P, is influenced by all adjacent nodal values. In the case where the nodes are defined at cell centers, the degree of influence is equal in all directions. Therefore, CD does not recognize the relative strength of influence of the flow direction. This may result in large errors or instabilities in flows that are dominated by convection or in cases where the grid spacing is large, i.e. large *Pe*. One way to reduce these errors is to use a finer grid.

2.3.2.2. Upwind Differencing (UW)

In upwind differencing (UD), quantities at the control volume faces are determined by assuming that the nodal value of the dependent variable ϕ represents an average value which holds throughout the entire cell. Thus the value of the variable at a particular face is set equal to its value at the nodal position in the upstream direction of the flow. In keeping with the illustrated example above, the value at the right hand face is given by

$$\phi_e = \phi_P, \text{ if } (\underline{u} \bullet \underline{n})_e > 0 \qquad [2\text{-}18]$$

$$\phi_e = \phi_E, \text{ if } (\underline{u} \bullet \underline{n})_e > 0$$

Where, $\underline{u}$ is the velocity vector and $\underline{n}$ is the direction normal to the face.

While UD is only accurate to first order of a Taylor series expansion, unlike the CD it identifies the influence of the flow direction and thus possesses unconditional convective stability. Therefore in strongly convection driven flows or at high *Pe*, the UD scheme is expected to perform better than CD scheme. However, since UD is only first order accurate, the resulting larger truncation error is manifested in the form of so-called false or numerical diffusion. This is particularly severe in situations where the grid is not aligned with the flow direction (Pantankar, 1980; Versteeg and Malasekara, 1995).

As the nodal positions get closer, the assumed piece-wise variation of ϕ from node to node becomes less important. Therefore, numerical diffusion can be reduced by refining the grid and by using structured grids. However as Versteeg and Malasekara (1995) have pointed out, the amount of grid refinement required to eliminate numerical diffusion is often prohibitively

expensive in terms of computational resources. In any case at low grid *Pe*, it might be better to resort to the CD scheme which possesses second order accuracy.

A Hybrid discretization scheme based on the combination of the central differencing and upwind differencing has been formulated. In region with low *Pe* numbers, the Hybrid scheme employs central differencing which is second order accurate and where high *Pe* numbers occur, upwind differencing which is accurate to first order, but accounts for the flow direction is used. Many authors have used this Hybrid differencing scheme for their simulations of flows in stirred vessels where the numerical grids are usually not uniform (Fokema et al., 1994; Brucato et al., 1998; Jenne and Reuss, 1999; Montante et al., 2001; Aubin et al., 2004).

2.3.2.3. Quadratic Upwind Interpolation (QUICK)

A higher order QUICK discretization scheme has been formulated which reduces the numerical diffusion created by upwind differencing, while at the same time avoids the instability associated with central differencing. The QUICK scheme obtains the face values of the dependent variable by fitting a parabola to values at three consecutive nodal points, the two nodes located on either side of the surface in question plus the next node on the upstream side. For the illustrated example, QUICK differencing gives the following expression:

$$\phi_e = \frac{3}{8}\phi_E + \frac{3}{4}\phi_P - \frac{1}{8}\phi_W \text{ , if } (\underline{u}\bullet\underline{n})_e > 0$$

$$\phi_e = \frac{3}{4}\phi_E + \frac{3}{8}\phi_P - \frac{1}{8}\phi_{EE} \text{ , if } (\underline{u}\bullet\underline{n})_e > 0 \qquad [2\text{-}19]$$

Therefore, the value at the control volume face has a larger degree of influence from the nodal positions in the upstream direction. In the formulation of QUICK differencing, unique upstream and downstream faces and cells need to be identified, restricting its use to structured grids.
Han et al (1981) made a comparison between the Hybrid (CD/UD) and QUICK schemes for simulating various flow types, which included laminar flow and turbulent re-circulating flows. By performing grid refinement, the authors found that predictions using the QUICK scheme on relatively coarse grids gave similar results as for the Hybrid scheme on fine grids. Therefore, they

concluded that more substantial savings in computational time and storage can be achieved by using the QUICK scheme than from further refinement of the grid.

2.3.2.4. Interpolation of the Time Derivative

For unsteady flow problems, the governing transport equations must be discretized in both space and time. Temporal discretization involves integration of the transport equation over a finite time step, Δt. If the spatially discretized part of the transport equation is represented by a function $F(\phi)$, the general transport equation can be written in the following form:

$$\frac{\partial \phi}{\partial t} = F(\phi) \qquad [2\text{-}20]$$

The time derivative can be approximated by the first order backward difference as follows:

$$\frac{\partial \phi}{\partial t} = \frac{\phi^{n+1} - \phi^{n}}{\Delta t} \qquad [2\text{-}21]$$

Where, ϕ^{n+1} is the value at the next time level, $t + \Delta t$ and ϕ^{n} is the value at the current time, t. The first order backward difference is adequate for most calculations; however, higher order differences can also be used if desired. Implicit or explicit methods have been developed to evaluate the above equation. The main difference between the two methods being whether $F(\phi)$ is evaluated at the current time level or at the new time level.

Upon discretization, the governing equations are reduced to the algebraic form:

$$a_p \phi_p = \sum a_{nb} \phi_{nb} + b \qquad [2\text{-}22]$$

The coefficients a_{nb} of the dependent variable at the neighbor nodes depend on the differencing scheme selected and include the effects of diffusion and convection. The term b includes the transient contribution from the previous time level and the pressure term. The coefficient a_p at

the considered nodal position consists of the sum of the neighbor coefficients a_{nb}, transient terms from the new time step and the variable part of the source term. To calculate the flow field, equations of this form need to be solved for the flow properties at each nodal point in the numerical grid.

2.4. Review of CFD Studies of Stirred Tanks

2.4.1. Grid Resolution

In three dimensional turbulent flow problems such as in stirred tanks, it is expected that the quality of the grid greatly influences the accuracy of the solution. In such cases, it is impossible to completely avoid discretization errors occurring due to the grid not being aligned with the flow direction. This situation is even more severe when unstructured grids are used. Therefore, structured grids have been used in most of the published studies.

As mentioned in Section 2-2, optimal grids are finer in regions where sharp gradients in flow properties are expected and coarser in places where relatively small changes occur. In impeller stirred tanks, sharp gradients in velocity, pressure and turbulence quantities k and ε are expected in the impeller stream and in the regions adjacent to the blades. Consequently, the grid should be more refined in these regions. The grid should also be adequately resolved in the 'no-slip' boundary regions near the impeller blades, shaft, baffles and tank wall in order to meet the limitations of the wall function formulations (Ng et al., 1998; Wechsler et al., 1999).

The error between the discretized equation and the exact solution of the governing partial differential equation is reduced when more control volumes are used in the solution domain. To determine the appropriate grid size, simulations must be carried out on successively refined grids, until no notable difference in the predicted values of important flow properties is observed. Versteeg and Malasekara (1995) pointed out that this systematic search for grid-independent results should be an essential part of any good quality CFD study.

Table 2-1: Numerical grids used in various studies in the literature.

Reference	*Tank Geometry, T=H (m)*	*Solution Domain*	*# of Cells*
Fokema et al., 1994	0.15	90°	17 200
Tabor et al., 1996	0.27	180°	120 000
Brucato et al., 1998	0.44	180 °	97 440
Jenne and Reuss, 1999	0.44	90°	194 500
Wechsler et al., 1999	0.15	90°	1 003 500
Bakker et al, 2000	0.30	90°	49 000
Ng and Yianneskis, 2000	0.10	180°	240 000
Lane et al., 2002	1.0	60°	43 900
Ranade et al., 2002	0.15	180°	630 800
Bartels et al., 2002	0.15	180°	2 082 800
Aubin et al., 2004	0.19	360°	155 000

Table 2-1 compares geometry sizes and grid densities used in various studies in the literature. It can be seen that there are still discrepancies as to the grid densities needed to adequately model the flow in stirred tanks. Most of the authors have reported good correlation between CFD and experimental values for the velocity fields in stirred tanks. However, turbulence quantities are not well predicted. It could be suggested that some of the grids presented in Table 2-1 have influenced these discrepancies between predicted and experimental values of turbulence flow properties.

Fokema et al. (1994) examined different grids ranging from about 7 000 to 54 000 control volumes by successively refining the grid in the impeller and baffle regions. The authors reported that the predicted flow noticeably differed when the grid was refined in the axial direction and concluded that grid independence was reached at approximately 17 200 volumes. However, it was not mentioned what flow property was used to examine the different grids in order to arrive at this conclusion. It should be noted that possibly a grid independent solution was not achieved on their finest grid since this is a relatively coarse grid and the level of successive grid refinement was small.

Brucato et al. (1998) compared four grid densities consisting of 2 646, 9 240, 29 106 and 97 440 cells. Results for the axial velocity showed that the smallest grid severely underestimated the recirculation intensity, while all other grids yielded results that differed marginally. The axial velocity close to the impeller also showed similar trends.

Ng and Yianneskis (2000) compared experimental values of the turbulent kinetic energy k, with the predictions of three different grids consisting of 46 016, 102 296 and 239 468 control volumes. The simulations were carried out on a calculation domain representing half the tank. All the grids calculated k values near the impeller which were much smaller than LDV values and calculations using the finer grids showed little improvement from the coarse grids. The authors attributed these discrepancies to deficiencies of the k-ε turbulence model. It should be noted, however, that the level of successive grid refinement was quite small and more grid refinement was necessary.

Ranade et al. (2002) also carried out grid sensitivity studies and found that in order to capture the trailing vortices, it is necessary to use more than 100 cells covering the impeller blades.
Ng et al. (1998) suggested that results that approach experimental data might be obtained with the k-ε turbulence model if 'unrealistically' large grids with over a million cells were used. Bartels et al. (2002) applied grids with approximately 2 million cells on a parallel-vector computer to simulate flow in a stirred tank using the k-ε turbulence model and a domain representing half the tank. Values of the power number for a wide range of Reynolds numbers representing both laminar and turbulent flow regimes were calculated. These values were in very good agreement with previously published experimental data. However, the necessary results for the velocity and turbulence fields were not reported.

In recent studies of Aubin et al. (2004), grid densities comprising of 76 000, 155 000 and 350 000 control volumes were tested. For the two finer grids qualitatively similar results were obtained for the axial profiles of the turbulent kinetic energy, however the results differed numerically by up to 12%. The profile predicted by the courser grid was different from the other two results, smaller by up to 25 %.

While it is generally accepted that using larger grid densities leads to more accurate predictions, optimization of a CFD analysis should also take into consideration the computational expense of a calculation and the associated calculation time.

2.4.2. Discretization Methods

Some researchers have investigated the effect of various discretization schemes on the accuracy of the predicted flow. Brucato et al (1998) performed simulations with the upwind hybrid (UD/CD) and QUICK discretization schemes, on a grid of about 97000 cells. The reported axial velocities obtained using these two schemes did not differ appreciably from each other. The authors concluded that for this grid size, "numerical diffusion effects associated with upwind scheme are not significant and that turbulent diffusion is largely dominant". The effect of the differencing scheme on the turbulence quantities was not reported. Montante et al (2001) also compared the effects of the Upwind Hybrid and QUICK schemes on the predicted flow in stirred tanks. They reported that the predicted flow field was identical for both schemes. However, it was not mentioned what property of the flow field was compared to arrive at this conclusion. Aubin et al (2004) investigated three differencing schemes- first order upwind, Hybrid and QUICK. The authors found that the type of differencing scheme had no effect on the mean velocities, although the first order upwind scheme was found to under-predict the swirling region below the impeller. Further comparison was made for the effects of differencing scheme on the turbulent kinetic energy. It was found that although all three schemes under-estimated the LDV turbulent kinetic energy data, the discrepancy was more severe in the case of the first order upwind, especially in the impeller discharge region with high velocity gradients and anisotropic flow.

2.4.3. Impeller Rotation Models

In a baffled stirred tank, the relative motion between the rotating impeller and the stationary baffles results in a cyclic variation of the calculation domain and thus presents a challenge to the numerical solution procedure. The literature demonstrates several different methods of modeling the impeller rotation.

2.4.3.1. Impeller Boundary Conditions Model

The most traditional approach to modeling the impeller rotation is to impose experimentally derived mean velocity and turbulence values in the impeller swept volume of the flow (Ranade and Joshi, 1989; Kresta and Wood, 1991; Gosman et al., 1992; Fokema et al., 1994; Brucato et al., 1998; Jenne and Reuss, 1999).

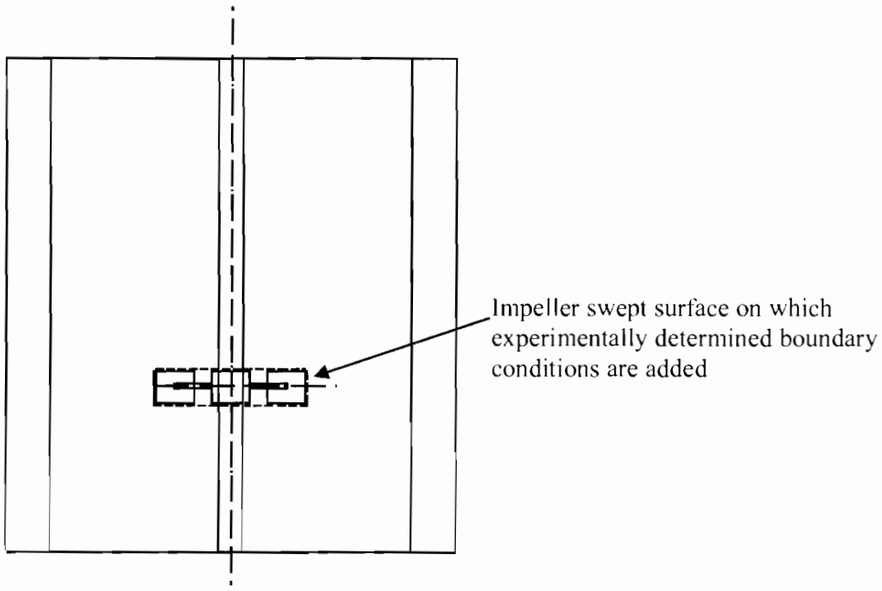

Figure 2-3: Impeller swept region of the stirred tank for specifying experimental boundary conditions.

The flow in the bulk of the tank is then calculated with these boundary values. This approach, referred to as the Impeller Boundary Conditions (IBC) method, therefore models the impeller implicitly. In most cases, time-averaged boundary values for all three velocity components as well as the turbulence quantities k and ε are specified and steady state conditions are imposed. The method by which the experimental boundary conditions are specified varies according to the type of impeller and the researcher.

Gosman et al. (1992) specified values of only the mean circumferential velocity, k and ε, in their simulation of the turbulent two-phase flow generated by a Rushton impeller. These values were applied throughout the volume swept by the impeller blades and not just the impeller swept surface. On the other hand Brucato et al. (1998), specified experimentally derived mean profiles of all three velocity components and the turbulent quantities k and ε, on the vertical cylindrical surface bounding the volume swept by the Rushton impeller. Ranade and Joshi (1989) modeled the axial flow pitched blade turbine impeller by specifying experimental values only on the bottom surface of the impeller swept volume. Fokema et al. (1994) modeled the same impeller as a thin disc with inlet boundary conditions on both sides. Experimental profiles of the velocity components and turbulence quantities as measured at the impeller discharge were prescribed on both these inlet boundaries

According to Marshall and Bakker (2003) it is usually sufficient to impose velocity and turbulence data along the edges of the impeller swept volume where the flow is discharged. In the case of the radial discharging Rushton impeller, prescribing boundary conditions on the vertical surface of the impeller volume is sufficient. For axial discharging impellers, it is suggested that boundary conditions should be specified on the top or bottom surface, depending on whether the impeller is up-pumping or down-pumping.

The main disadvantage of the IBC method is that since experimental data is needed, it is not fully predictive. Because the flow generated by any impeller type is also dependent on the geometric configuration of the vessel and on operating conditions, experimental data is required for each specific case under investigation. Studies conducted to investigate the sensitivity of CFD simulations to the impeller boundary conditions imposed demonstrated that numerical predictions show a strong sensitivity to the impeller boundary conditions and satisfactory predictions rely on the availability and accuracy of these for each vessel configuration under investigation (Fokema et al., 1994; Brucato et al., 1998). Therefore, it can be concluded that there is no general empirical boundary condition model for a particular impeller type, without consideration of the rest of the vessel configuration.

The impeller boundary conditions method also has the disadvantage that, since the impeller is not explicitly modeled, details of the flow structures behind the blades are not resolved by the simulation. These details are important in the study of flows such as gas-liquid mixing, where the gas tends to accumulate in the low pressure trailing vortex structures behind impeller blades (Van't Riet and Smith, 1975; Ranade and Van Den Akker, 1994). A good understanding of the trailing vortex structure is also important in chemical reacting flows as the vortices affect the blending performance of impellers (Escudié et al., 2003).

2.4.3.2. The Snapshot Model

Ranade (1997) has proposed the so called "snapshot" approach that attempts to capture details of the flow both around and outside the impeller blades without knowledge of any empirical data. The characteristic of the impeller discharge flow is determined by the shape of the impeller blades through generated pressure and centrifugal forces. The impeller rotation induces suction of the fluid at the back side of the blade and ejection of the fluid on the front side. In the

computational snapshot approach, this phenomenon of suction and ejection is modeled by specifying appropriate momentum source and sink terms at the front and back side of the blade, respectively. In this approach, fully developed flow conditions are assumed and steady state calculations are carried out in a fixed reference frame. The geometry of the impeller is explicitly modeled and the impeller is considered as fixed at a particular instance. Repeated calculations using different impeller positions can then be averaged to get the final phase average flow field. The snapshot method can be generalized to simulate impellers of any shape, with just the knowledge of the impeller geometry and rotational speed.

Through plots of the predicted turbulent kinetic energy contours at the impeller center plane and contours of the predicted z-vorticity at a z-θ plane, Ranade et al. (2002) were able to show the ability of the snapshot approach to qualitatively capture the effects of the trailing vortices behind the blades of a Rushton turbine. The computational snapshot approach has also been extended to predict the flow in stirred tanks agitated by a dual Rushton turbine impeller by Deshpande and Ranade (2003). The objective of their work was to evaluate whether the specification of source/sink terms could capture the interaction between multiple impellers. It was found that for sufficiently separated Rushton turbines, each turbine generated its own characteristic upper and lower ring vortex and for low separation, the impeller streams from both turbines merged to form two large ring vortices, in accordance with experimentally observed results.

The results described above are encouraging, however Luo et al. (1993) have pointed out that the method of representing the impeller rotation by sources of momentum contains many uncertainties as to the magnitude of body forces and how these are distributed over the impeller blade.

2.4.3.3. Multiple Reference Frames Model

The Multiple Reference Frames (MRF) model employs the fact that in a baffled stirred tank where the clearance between the impeller blades and the baffles is comparable with the impeller diameter, the fully developed flow in the vicinity of the impeller is not affected by flow conditions in the rest of the tank. Therefore for all practical purposes, at a certain radial distance from the impeller steady-state conditions can be assumed both in a rotating and stationary reference frame (Tabor et al., 1996). At this radial distance, the tank geometry is divided into an inner region containing the rotating impeller and an outer region with the stationary baffles.

In the impeller region, steady state calculations are performed in a frame of reference rotating with the impeller. In this way, the effect of the blade rotation is accounted for by virtue of the frame of reference, allowing for the explicit modeling of the impeller geometry. In the outer region, steady-state calculations are performed in the stationary frame of the tank wall and baffles. The calculations in the impeller and bulk regions are performed simultaneously and the flow variables at the interface are made equal in both the rotating and stationary reference frames. On adequate grids, the MRF model is able to capture details of the trailing vortex structures behind the impeller blades and results have been comparable to the more accurate time-dependent method described in the following section (Tabor et al., 1996; Bartel et al., 2002).

The Inner-Outer (I-O) method provides a slight variant to the MRF model. In this approach, the solution domain is divided into two partially overlapping regions. The simulation is started with a steady state calculation of flow in the inner volume, using a frame of reference rotating with the impeller, with still-fluid boundary conditions imposed on the outer surface.

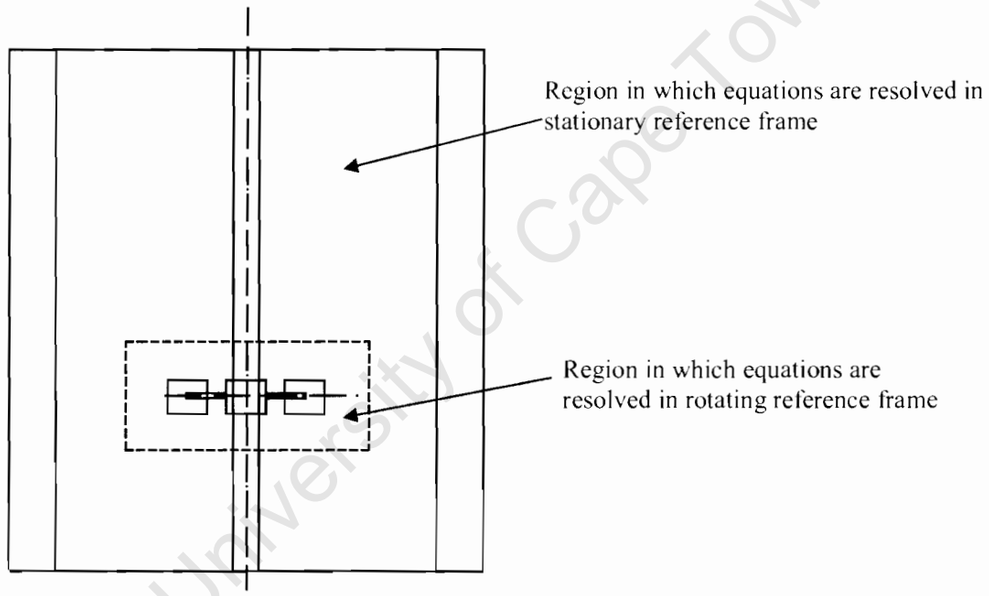

Figure 2-4: Regions of rotating and stationary frames of reference of flow calculation.

From the inner calculation, values for the velocities and turbulence quantities are obtained on the surface of the impeller swept volume. The values are translated into a stationary frame and are then used as boundary conditions for simulation of flow in the entire tank. The results of the outer

calculation are then translated into a rotating frame and used as boundary conditions at the outer surface of the inner zone and used for a second inner calculation. This procedure is repeated until no difference is observed between subsequent impeller boundary conditions. This approach was used by Harvey et al. (1996-1997), Brucato et al. (1998) and Montante et al. (2001). No studies have been reported in the literature comparing the I-O approach with the MRF method. Therefore the merits of one over the other are not clear. However since the I-O approach involves successive simulations to obtain boundary conditions, it probably requires a longer time to get a converged solution.

The impeller models described in the preceding sections have all imposed steady-state conditions on the fully developed flow. Experimental studies have however shown that there is a strong unsteady periodic component to the flow associated with the frequency of the impeller blade passage (Yianneskis et al., 1987; Wu and Patterson, 1989; Lee and Yianneskis, 1994; Escudié et al., 2004). In the vicinity of the impeller, the component of the flow associated with the periodic fluctuations of the blades is quite significant and has to be included in the analysis of the different flow variables (Luo et al. 1993; Montante, 2001). Knowledge of this periodic component is also helpful in understanding the respective roles of the different flow components in macro and micro mixing, and in formulating more accurate estimates of the turbulence quantities. According to Lee and Yianneskis (1994), steady-state predictions can suffer inaccuracies as they do not take into account this periodic passage of the blade. Time-dependent calculations should therefore be the most accurate way of representing the flow induced by a rotating impeller in a baffled stirred tank.

2.4.3.4. Sliding Mesh Model

The sliding mesh approach presented by Luo et al. (1993) involves the solution of the full time-dependent form of the transport equations. The calculation domain is also divided into two regions as in Figure 2-4. Lee and Yianneskis (1994) reported that for a tank stirred by a Rushton turbine, the region of flow affected by the periodic passage of the blades extends to a radius of half the impeller diameter away from the blade tips and 1.5 blade heights above and below the impeller disc. Therefore, in the sliding mesh formulation, the inner region must encompass this zone. At the interface between the two regions, the computational grid of the inner region is allowed to slide relative to outer region as the calculation progresses in time. In this way the

impeller geometry is explicitly modeled. The motion of the grid is not continuous but is in discrete time steps. In each region, equations are solved in the respective frame of reference at each time step, and data is interpolated from the rotating to the stationary region taking into account the relative motion.

Being time dependent, the sliding mesh method is the most accurate representation of the actual phenomenon of the impeller rotation. Unfortunately, this also makes it more computationally demanding resulting in calculation times which can be an order of magnitude longer than the steady state models. Luo et al. (1993) compared mean velocity profiles predicted by the SM method with experimental data and found that the agreement was good, despite the fact that a relatively small grid size was used. Owing to advances in computers, the sliding mesh method has been more widely used in the more recent studies (Ng et al., 1998; Ng and Yianneskis, 2000; Bakker et al., 2000; Montante et al., 2001; Bartels et al., 2002; Aubin et al., 2003).

2.4.3.5. Comparison of Impeller Models

Several researchers have conducted studies to compare the various impeller modeling methods. Brucato et al. (1998) conducted a comprehensive comparison of alternative impeller modeling approaches. Although the turbulence levels were underestimated by all the models, it was found that the SM approach gave the best agreement with experimental data for both the mean velocities and turbulence levels. This under prediction of turbulence has also been reported by several other authors, for example Luo et al. (1993), Tabor et al. (1996), Ng et al. (1998) and Montante et al. (2001).

Tabor et al. (1996) validated both the SM and the MRF techniques against experimental data for the flow generated by a Rushton turbine. Both the SM and MRF approaches gave qualitatively good results. Interestingly, the MRF achieved the best quantitative comparison with experimental data when a large number of control volumes were used and the SM calculation over-predicted the mean velocities. Montante et al. (2001) compared the SM and the IO modeling methods. Unlike previous IO simulations, the authors added to the turbulent kinetic energy a term representing the periodic fluctuation resulting from the blade passage. The predicted results of the SM method and the IO methods were very similar. Similar work was conducted by Aubin et al. (2004), for the flow generated by a down-pumping and an up-pumping pitched blade turbine. The

results showed that the choice of modeling approach, SM or MRF, only slightly affects the mean flow field in the impeller discharge region. In the rest of the tank, results were comparable.

2.4.4. Turbulence Models

In most numerical studies, turbulence in stirred tanks is modeled by the standard k-ε model as presented by Lauder and Spalding (1974), even though it is known that this method of modeling turbulence may fail in flows with strong streamline curvature and vortex generation. This choice is probably made as a compromise between computational expense and solution accuracy. Some workers have however reported velocity distributions using this method, which compare adequately with experimental data. For example Ranade et al. (1989) presented predicted profiles of radial and axial velocities in both the near impeller and bulk regions of the tank, which were in good agreement with LDV data. However, some lack of quantitative correlation in the predicted values of tangential velocity and turbulent kinetic energy was observed.

In their assessment of the sliding mesh impeller method, Ng et al. (1998) found that predictions using the standard k-ε turbulence model underestimated the experimental values of turbulent kinetic energy near the impeller, although values away from the blades were well predicted. Mean velocity data across the entire vessel was in good agreement with the experimental data. Montante et al. (2001) used the SM and the I-O impeller models with the standard k-ε model to investigate the dependency of flow on impeller clearance from the tank bottom. In all cases, they reported very good agreement between LDV and numerical data for velocity profiles in the tank. Profiles of turbulent and total kinetic energies however indicated a severe under prediction of turbulence levels. Simulations using the snapshot impeller approach and standard k-ε model for turbulence have also shown good agreement for velocities and a general under prediction of the turbulent kinetic energy (Ranade et al., 2002; Deshpande and Ranade, 2003). Other workers using the standard k-ε turbulence model with various impeller models also reported a general underestimation of the turbulence levels (Brucato et al., 1998; Aubin et al., 2003; Jaworski and Zakrzewska, 2002).

Several studies have focused on the effects of the turbulence model on the numerical predictions of flow in stirred tanks. Most commonly a comparison between different variations of the k-ε model has been made. Ranade and Joshi (1989) investigated a parametric sensitivity of the

empirical constants used in the k-epsilon model, by applying empirical constants for re-circulating flows suggested by Abujelala et al. (1984). They found that these constants have a degree of influence on the predicted k values, although the results were still lower than experimental data. Jenne and Reuss (1999) have compared three variations of the k-ε model, namely the standard k-ε, Chen-Kim k-ε and RNG k-ε. The results using the standard and optimized Chen-Kim models showed the best quantitative correlation with experimental data for the mean velocities. However the authors have not reported any quantitative data on the predicted turbulence levels. Jaworski and Zakrazewska (2002) also compared different variants of the k-ε model: standard, realizable, Chen-Kim, optimized Chen-Kim, as well as the RSM, and got the similar results as Jenne and Reuss (1999). Profiles of turbulent kinetic energy obtained with all the models underestimated the experimental values, with the standard k-ε model showing the smallest deviation from experimental data. The results obtained by Aubin et al (2004) also showed that the standard k-ε and RNG k-ε models produced similar under-prediction of the turbulent kinetic energy, especially in the impeller discharge stream where the flow is expected to be highly anisotropic.

It is generally suggested that a turbulence model that is not based on the assumption of isotropic turbulence would give better results. However, in the study conducted by Jaworski and Zakrazewska (2002) the Reynolds Stress Model (RSM) based on anisotropic turbulence, produced lower values of turbulent kinetic energy than the standard k-ε model. This result was also observed by Montante et al. (2002).

With current capabilities in computing power and memory, the use of Large Eddy Simulation techniques in numerical studies of flow in stirred tanks is becoming more popular. Some relatively older work that deals with the use of LES techniques to model turbulent flow in a stirred vessel is that by Eggels (1996). The impeller rotation was modeled by means of a varying force field in space and time, and calculations were performed on grids of up to approximately 14 million grid points using a scheme called a Lattice-Boltzman scheme. It took approximately 85 hours on an advanced computer to reach a converged solution. The predicted velocity profiles were in excellent agreement with previously reported LDV data. Derksen and Van Den Akker (1999) also used the same approach as Eggels (1996). They presented predicted turbulent kinetic energy levels that were in good agreement with experimental data. More recently, Hartmann et al., (2004) have also presented results of simulated flow in stirred tanks using LES, which show very good agreement with experimental data for both the mean velocities and the turbulent kinetic

energy. Due to the large grid resolutions required and the associated computational expense, LES techniques are probably still limited to research purposes and have not been fully adopted as an engineering design tool.

While the general underestimation of the turbulence levels observed by various researchers may have been due to inadequacies of the k-ε turbulence models, the influence of other model parameters (e.g. grid resolution, discretization schemes and impeller model) cannot be ruled out.

CHAPTER 3 CFD METHODOLOGY

The CFD software *Fluent* was used to predict the flow of a single phase fluid in an impeller stirred tank. *Fluent* is a general purpose CFD solver that uses finite volume techniques to solve the set of transport equations of fluid flow. In this chapter, the stirred tank model and numerical solution procedures adopted are described, followed by a brief discussion of the experimental data used to validate the predicted flow.

3.1. Model Description

3.1.1. Stirred Tank Configuration

The system investigated in the present study is the standard configuration stirred vessel consisting of a cylindrical tank with four equally spaced vertical baffles and agitated by a Rushton turbine impeller (c.f. Figure 3-1). This geometry represents more or less a research standard, for which considerable experimental and numerical data is available in the literature. Computations were performed for a laboratory scale system with tank diameter of 0.15m and other ratios as shown in Figure 3-1.

In most industrial applications, impeller agitated tanks are used in mixing processes involving multi-phase substances. However, since the main focus of the present study was on numerical models, the less complex case of a single phase fluid was investigated. A range of impeller speeds corresponding to Reynolds number, $\mathrm{Re} = \frac{\rho N D^2}{\mu}$ covering the laminar and turbulent flow regimes ($0.5 \leq \mathrm{Re} \leq 60\,000$) were simulated. In the laminar Reynolds number range ($0.5 \leq \mathrm{Re} \leq 7000$), the instantaneous transport equations for mass and momentum were solved and in the higher Reynolds number range, the Reynolds averaged equations with k-ε turbulence models and standard wall functions presented in Equations 2-13 to 2-14 were used.

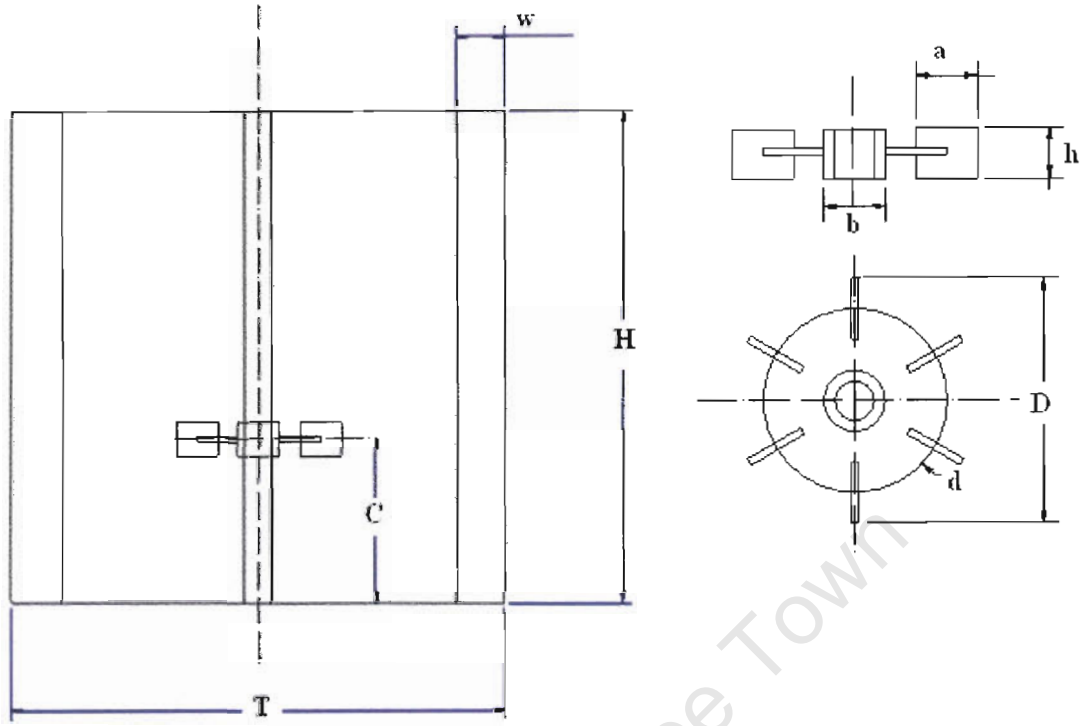

H/T	C/T	w/T	D/T	d/D	a/D	h/D	b/D
1	1/3	1/10	1/3	3/4	1/4	1/5	1/5

Figure 3-1: Stirred tank and Rushton turbine model dimensions.

3.1.2. Computational Grid Generation

The calculation domain and computational grids were generated with the commercial grid generation tool *Gambit (Fluent, Inc)*. Since the stirred tank and expected flow show rotational symmetry of two periodic repeats, it was only necessary to perform calculations on a model that represents half the vessel geometry (i.e.180 degree in circumferential direction) by applying periodic boundaries. This significantly reduced the cost of the calculation in terms of computer memory and calculation time.

The underlying geometry of the stirred tank was defined by the multi-block arrangement shown in Figure 3-2 using *Gambit* geometry creation tools. The construction of the geometry using this multi-block arrangement provides more flexibility in generating locally structured grids with

hexahedral body fitted control volumes and also facilitates the placement of additional nodes in specific regions where high flow gradients occur. Physical boundaries of the flow domain conformed to the faces of the blocks and thus the impeller blades, disc and the baffles were modeled as infinitely thin surfaces between adjacent blocks.

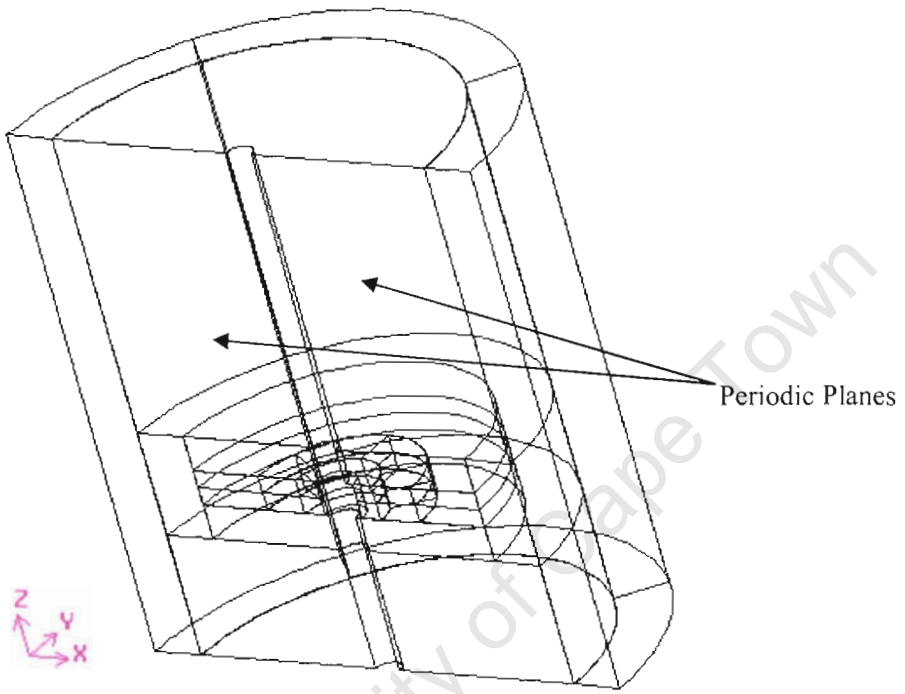

Figure 3-2: Block structure arrangement defining calculation domain.

The grid density was specified using the mesh-seed technique. In this technique, the number of control volumes in a particular region is set by specifying the number of nodal points on edges in the r, θ and z directions. In the region encompassing the impeller discharge stream (contained within 1.5 blade heights above and below the impeller and extending horizontally across the tank diameter), the grid density was increased because large gradients in flow properties are expected (c.f. Figure 3-3). In order to resolve the vortex structures generated behind the impeller blades, the largest node density was placed along the edges of the blade surfaces and in the circumferential direction of the geometry. The grids were also refined near the baffle surfaces to resolve any vortices formed in this region of the flow.

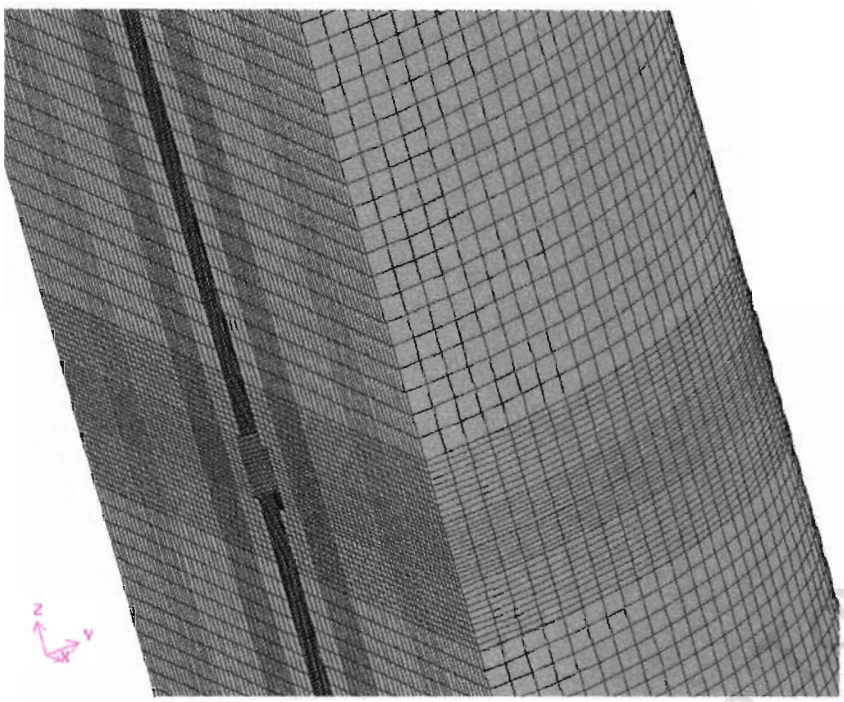

Figure 3-3: Meshed model showing local grid refinement in the impeller stream region.

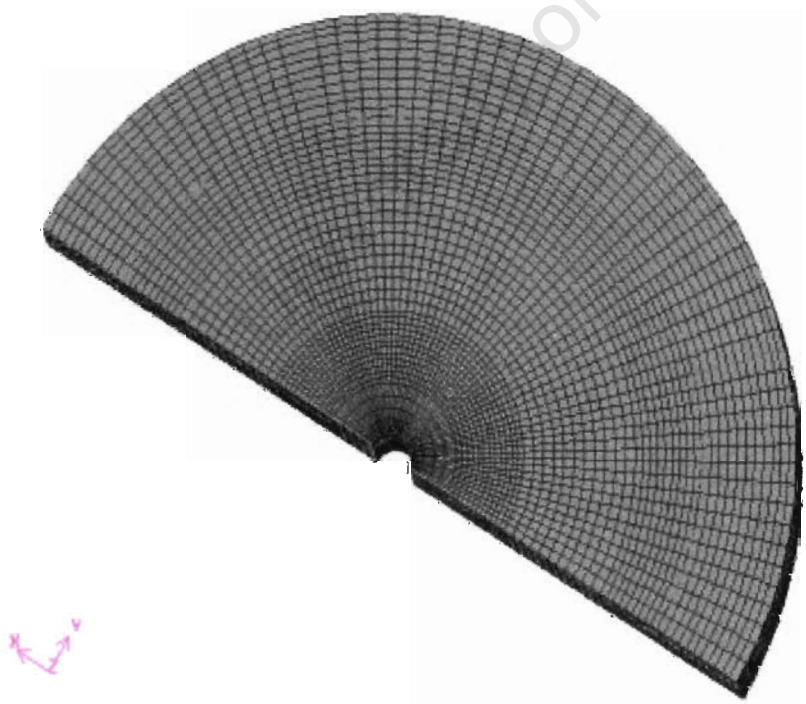

Figure 3-4: Plan view showing fine grid resolution in the circumferential direction of the tank model.

The reliability of CFD predictions depends on the quality and size of the grid used. Grid dependency studies were performed by systematically increasing the number of control volumes in the radial, axial and circumferential directions of the calculation domain and comparing the calculated flow properties. The four grid levels described in Table 3-1 were compared.
When refining the grid, care was taken to ensure that the different grids had the same relative distribution of control volumes in the various regions of the tank.

Table 3-1: Grid models used in present study.

Distribution of Control Volumes					
	Radial	Axial	Azimuth	Blade r × z	Total
Grid 1	22	42	36	6 × 8	~ 33 000
Grid 2	41	84	66	12 × 16	~ 230 000
Grid 3	63	126	102	18 × 24	~ 800 000
Grid 4	84	168	136	24 × 32	~1 900 000

3.1.3. Boundary Conditions

Prior to solving the closed set of transport equations, values of the dependent flow variables need to be specified on the calculation domain boundaries in order to get a unique solution for the particular case being investigated. It was therefore necessary to specify boundary conditions on the tank walls, baffles, impeller components and periodic planes.

Boundary Conditions on Solid Surfaces

Solid surfaces bounding the flow domain were modeled as impermeable walls with negligible wall roughness (c.f. Figure 3-5). 'No-slip' boundary conditions were specified for the fluid at the solid surfaces. This condition assumes that fluid particles stick to the wall and assume the velocity of the wall. In the turbulent flow calculations, the 'no-slip' boundary conditions were defined according to the wall functions presented in Chapter 2.

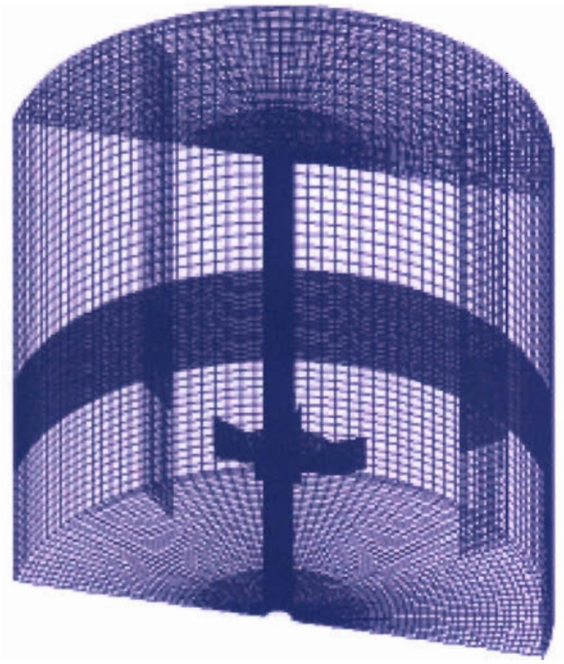

Figure 3-5: Impermeable wall boundary surfaces of the flow domain.

Boundary Conditions on Periodic Planes

Cyclic boundary conditions were imposed on the periodic planes (c.f. Figure 3-2). The flow at a cyclic boundary is treated as though the opposing periodic plane is a direct neighbor to the fluid adjacent to the first periodic boundary. In this way, the flow entering the calculation domain through a periodic boundary is identical to the flow exiting through the opposite periodic plane. The periodic planes are in fact part of the interior fluid domain and no additional boundary conditions are required except the one-to-one correspondence between the nodal values on the two planes.

3.1.4. Discretization Schemes

In the grid dependency study, simulations were performed using the first order upwind discretization scheme. In order to investigate the effect of discretization scheme on the predicted flow properties, computations were also conducted using the higher order central and QUICK discretization scheme on the finest grid consisting of 1 900 000 control volumes. From these results, the most accurate discretization scheme was established and used to compare different impeller and turbulence models.

3.1.5. Impeller Modeling Methods

As mentioned in the preceding chapter, one of the challenges of modeling flow in a baffled stirred tank is the treatment of relative motion between the rotating impeller blades and the stationary baffles. Various methods developed to model this relative motion were discussed. In the *Fluent* solver, the steady state Multiple Reference Frames (MRF) and the transient Sliding Mesh (SM) models are available for treating this rotor-stator interaction. In the present study, the influence of impeller modeling method on the numerical solution of flow was investigated using these models.

3.1.5.1. Multiple Reference Frames Model

This method required defining a region in the solution domain encompassing the impeller and the flow around it, where flow equations are solved in a rotating reference frame. In the rest of the domain surrounding this impeller region, calculations were performed in the stationary reference frame. Published LDV data Lee and Yianneskis (1994) indicates that the region where flow is strongly influenced by the periodic passage of the blades extends to a radius of D/2 away from the impeller tip and 1.5 blade heights above and below the impeller disc. The solution domain was divided such that the impeller region extends to these bounds, thus encompassing the region of flow affected by the periodic passage of the blades. In the rotating reference frame region, solid walls were assigned zero velocities relative to the impeller and coordinate rotation.

Steady-state transport equations were solved in the impeller region using a frame of reference rotating at the impeller speed, with no grid movement. The velocity vectors in the stationary and rotating reference frames, u_i and V_i respectively, were related by:

$$u_i = V_i + \in_{ijk} \omega_j x_k \qquad [3\text{-}1]$$

where, ω_i represents the angular velocity component, x_i the position relative to the rotation axis and $\in_{ijk}$ the cyclic permutation symbol. The effects of Coriolis and centrifugal forces on a fluid particle were accounted for by the additional source term F_i.

$$F_i = \rho \in_{mni} \left(2u_m \omega_n - \omega_m \left(\in_{pqn} \omega_p x_q\right)\right) \qquad [3\text{-}2]$$

Equations in the rest of the tank were resolved in the normal inertial form presented in Chapter 2. During the calculation, the solutions in the stationary and rotating reference frames were coupled by assuming that absolute velocity values at the interface were equal in both regions. This is an approximation that applies to tank geometries with sufficient spacing between the impeller blades and the baffles.

3.1.5.2. Sliding Mesh Model

In the transient SM computations, the same bounds as the MRF model were used to define the impeller region. However, because the transient calculations required significantly more computing time, a further attempt to reduce the computational cost was made by performing calculations on a model representing a 60 degree section of the vessel, with one impeller blade and one baffle. In reality, this models a tank with six wall baffles and is not a true representation of the standard four-baffle configuration. However, the purpose of the wall baffles is to prevent solid-body rotation and once this is achieved, the addition of more baffles should not make much difference to the flow patterns in the stirred tank, except locally near the baffles (Tatterson, 1991). Further, a comparison of steady state MRF solutions on the 180 and 60 degree models showed that there was no notable difference in the flow calculated with these geometries. This approach was also taken by Lane et al. (2002) who compared gas-liquid flow measurements in a standard four-baffle stirred vessel with numerical predictions of a 60 degree model.

The SM technique is perhaps the most realistic approach for modeling flow in stirred tanks, since it takes into account the transient behavior of the flow, especially the inherent periodic unsteadiness due to the passage of the impeller blades. This is achieved by allowing the inner rotating reference frame zone to slide relative to the stationary zone along the grid interface in discrete time steps. At each time step, time dependent calculations are performed in both the impeller and outer region, using the respective frame of reference and a conservative interpolation was used to obtain flow variables and face fluxes across the interface.

Implicit time-stepping was used to discretize the transient terms in the transport equations. The coupling between the flow solutions on either side of the interface was treated implicitly, taking into account the fact that the connecting cells change due to the sliding action. The size of the time step is crucial to the accuracy of the transient calculation since this determines details of the

transient features captured. Due to time constraints, no attempt was made to investigate the effect of time-step size on the predicted values. However, a conservative size of 1×10^{-4} seconds was used for the finest grid level in Table 3-1. On this grid, each time step corresponds to a sliding movements of no more than one circumferential face at the interface.

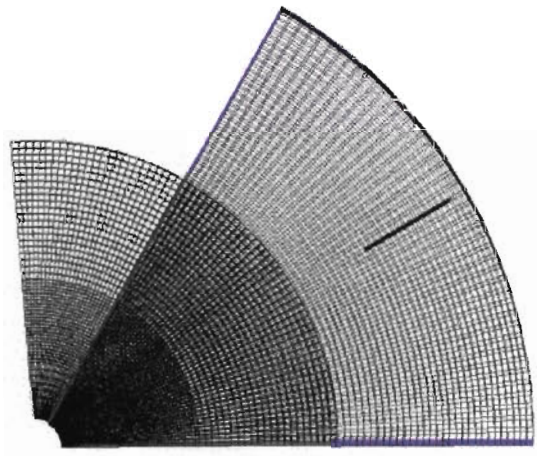

Figure 3-6: Sliding action of the inner solution region on 60 degree geometry.

The fully developed flow conditions in a stirred tank reach a pseudo-steady state in which the flow variables show a periodic variation which is a function of the blade frequency (Campolo et al. 2003). Starting with a fluid at rest, SM computations require a substantial amount of computing time to overcome the start-up flow before the pseudo-steady state condition is achieved. In order to shorten this start-up time, the SM calculations in the present study were started from a flow field predicted by the MRF model.

3.1.6. Turbulence Models

For most of the study, the standard k- ε turbulence model was used. The limitations of the standard k-ε turbulence model for predicting swirling or re-circulating flow has been documented (Abujelala et al., 1984; Jenne and Reuss, 1999). It has also been generally accepted from previous studies that prediction of flow in stirred tanks based on the standard k-ε model results in a substantial underestimation of the turbulence levels in the impeller stream. One of the objectives of the present study was to evaluate whether this discrepancy in predicted and measured turbulence levels is a result of adequacies in the standard k-ε turbulence model or due to

numerical inaccuracies. In addition to the standard k-ε turbulence model, computations were also conducted using the RNG- k-ε turbulence model and the anisotropic Reynolds Stress Model. However with the Reynolds Stress Model, attempts to reach a converged solution were not successful. Therefore, the study was limited to the two isotropic k-ε models.

3.2. Solution Procedure

Since the discretized equations contain non-linear terms of the dependent variable, and are highly coupled, iterative methods were employed. Furthermore, while pressure appears in the momentum transport equations, there is no transport equation for the pressure field (although the momentum and continuity equations can be combined to derive an equation for the pressure). Different strategies have been proposed for the treatment of this pressure-velocity coupling and the nonlinearities in the discretized equation set.

The Semi-Implicit Method for the Pressure Linked Equations (SIMPLE) family of algorithms (SIMPLEC, SIMPLER, PISO) has been widely used to resolve both the problems associated with the nonlinearities in the equations and the pressure-velocity coupling. In these methods, the discretized momentum equations are solved using a guessed pressure field. The velocities obtained in this way will not satisfy the continuity equation and velocity correction expressions are proposed. These expressions are substituted into the discretized continuity equation from which pressure correction equations are derived. The pressure correction equations are substituted back into the momentum equation to continue this iterative process until continuity is satisfied. The different variants of the SIMPLE algorithm vary in the way the velocity correction expressions are derived from the discretized equations. Details of the derivations of the algorithms can be found in Patankar and Malasekara (1980) and Versteeg (1995).
For the steady-state MRF calculations, the SIMPLEC algorithm was employed and for unsteady SM calculations, the PISO algorithm was used as this algorithm has been reported to be more robust for transient calculations (Ranade, 2002; Fluent 6.1 User's Guide, 2003)

Convergence Monitoring

Since the solution of the discretized equation is an iterative process based on guessed initial values, there is an imbalance between the right hand side and left side of the equation. This imbalance represents the error or residual in the final iteration solution of the equation over the

control volume. The total residual is the residual summed over all control volumes in the computational domain. For the MFR model, the solution was considered converged when the total residuals for the discretized continuity equation, scaled by its largest absolute value over the first 5 iterations, dropped to about 1×10^{-4} (c.f. Figure 3-7). The time required to reach convergence was dependent on the discretization scheme, with the QUICK scheme calculation requiring the most time.

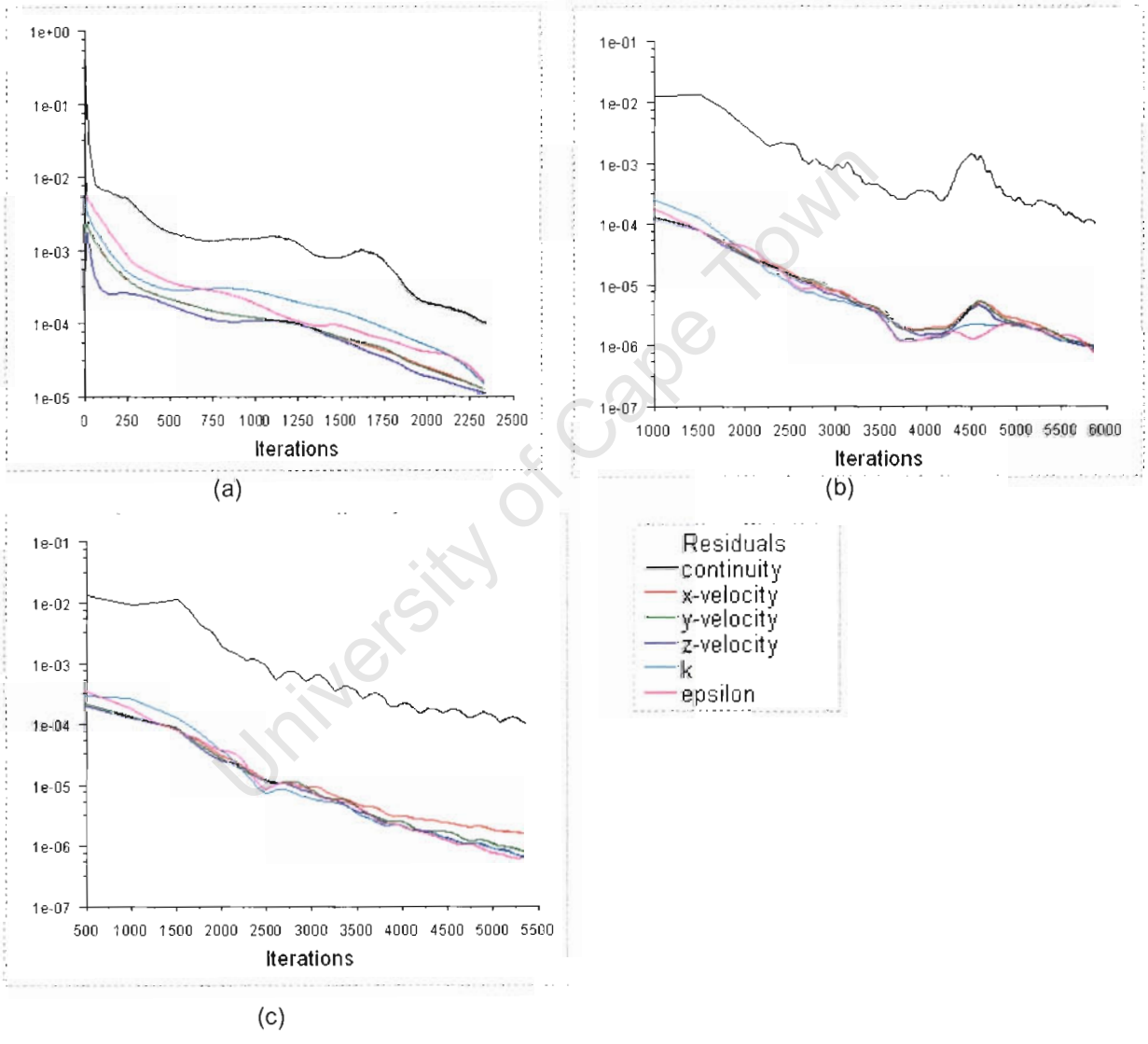

Figure 3-7: Residual convergence for (a) First order upwind, (b) Central and (c) QUICK discretization schemes-SIMPLEC algorithm on Grid 4.

In the case of the SM computation, convergence towards pseudo-steady state was assumed when the torque on the impeller and shaft showed no significant difference between consecutive periods of rotation. Figure 3-8 shows the time variation of the torque coefficient during the computation.

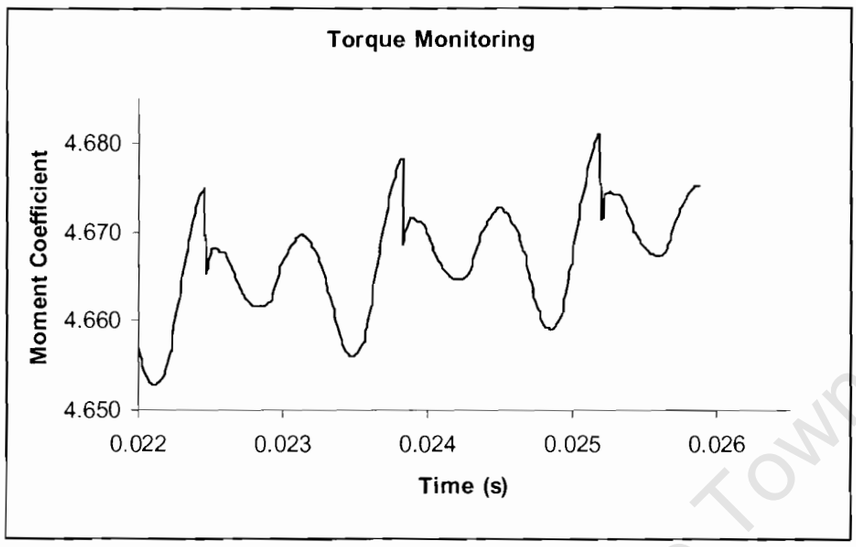

Figure 3-8: Torque convergence monitoring for sliding mesh simulation.

3.3. CFD Model Validation

3.3.1. Power Numbers

The power drawn by a rotating impeller is of vital importance for the process and mechanical design of the stirred tank. Rushton et al. (1950) carried out dimensional analysis and showed that

$$N_p = f\left(\mathrm{Re}, Fr, \frac{T}{D}, \frac{H}{D}, \frac{w}{D}, etc\right) \qquad [3\text{-}3]$$

where $N_p = P/(\rho N^3 D^5)$ is the Power number, $Re = (\rho N D^2)/\mu$ is the Reynolds number and $Fr = (N^2 D)/g$ is the Froude number. They argued that since Fr number is a ratio of gravitational forces and centrifugal inertial forces, then for geometrically similar baffled stirred tanks in which no central vortex occurs, Equation [3-3] could be reduced to

$$N_P = f(\mathrm{Re}) \qquad [3\text{-}4]$$

By conducting experiments in which the Power requirement P was measured for different impeller speeds N, the functional relations for different impellers were determined. These experiments were conducted in different sized geometrically similar stirred tanks and the data was presented in the form of log-log plots of N_p versus Re. Figure 3-9 shows a sketch of the typical power curve obtained by Rushton et al. (1950).

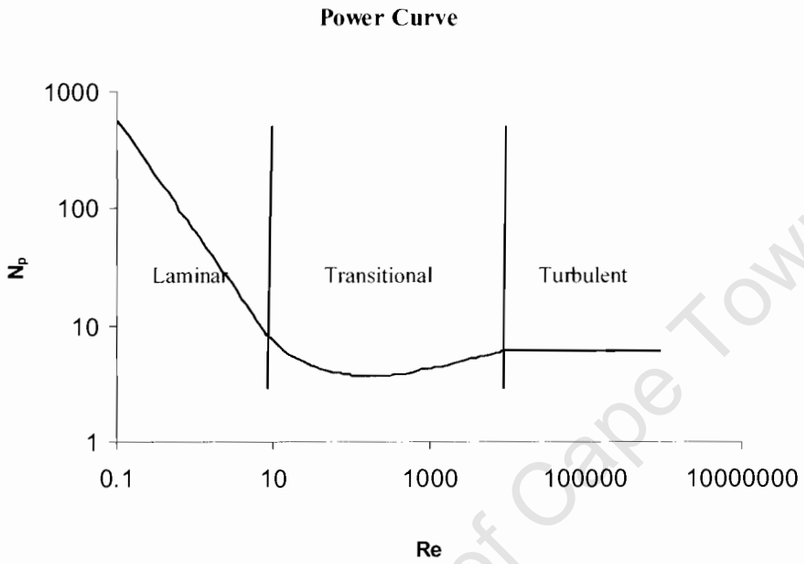

Figure 3-9: Typical Power number curve of Rushton et al. (1950).

In the laminar Re range ($\mathrm{Re} \leq 10$), N_P and Re were found to be related by the following equation:

$$N_P = \frac{K}{\mathrm{Re}} \qquad [3\text{-}5]$$

where K is a constant that depends on the system geometry. In the turbulent Re number range, ($\mathrm{Re} \geq 10^4$), the relation was:

$$N_P = A$$

The constant A was dependent on the impeller type. Between the laminar and turbulent Re numbers, a transition zone was identified in which no simple mathematical relation exists between N_p and Re.

In the present study, simulations were performed for a range of impeller speeds covering laminar, transition and turbulent Reynolds numbers and the corresponding Power numbers were calculated and validated against the results of Rushton et al. (1950).

3.3.2. Velocity and Turbulent Kinetic Energy Profiles

Wu & Patterson (1989) have presented one of the most extensive LDV data set of flow variables in the impeller stream of stirred tank. They presented axial profiles of the mean and RMS values of the three velocity components at various radial distances from the impeller tip. For a more detailed validation of the CFD model, the predicted flow was compared with this data. It should be noted that the experimental studies of Wu and Patterson, (1989) were conducted in a larger unit of similar geometrical configuration and results are reported for Re = 29 000. The quantitative comparisons are however valid for the turbulent Re numbers investigated in the present study. Wu and Patterson (1989) reported that for different impeller speeds in the turbulent flow regime, profiles of the velocity components normalized by the impeller tip velocity (πND) were identical. Independent studies by Costes and Cordec (1988) and Dyster et al. (1993) also found that for turbulent flow, velocity values normalized by the impeller tip speed were independent of the rotational speed of the impeller and of the size of the unit.

Comparison of the MRF predictions with the data of Wu and Patterson (1989) depends on which region of the calculation domain was being sampled. In the inner region in which equations are solved in a rotating reference frame, it is necessary to take circumferential averages of the flow field. According to Tabor et al. (1993), this approximates repeated sampling of the flow field as the impeller rotates. Since the fully developed flow reaches a periodic state, the SM solution was sampled at successive time-steps and the average taken.

CHAPTER 4 RESULTS AND DISCUSSION

4.1. Large Scale Flow Fields

A qualitative validation of the predicted large-scale flow was achieved by plotting vectors of the mean velocity and contours of the turbulent kinetic energy at various planes through the stirred tank. For a more quantitative validation, Power numbers for a range of impeller speeds were also calculated. The bulk flow patterns obtained with the different models investigated showed very similar trends when compared with one another as well as with documented experimental observation. In the following section, mean velocity vectors, turbulent kinetic energy contours and Power numbers obtained with the MFR and standard k-ε turbulence model are presented.

4.1.1. Mean Velocity Fields

Figures 4-1 shows mean velocity vectors on vertical planes located at different angular positions before a plane of a baffle, obtained with the grid consisting of 230 000 control volumes and the upwind discretization scheme. The vector plots show the typical flow patterns observed for a Rushton turbine: the fluid is drawn into the impeller axially, deflected in a radial direction and then discharged from the impeller at a high speed radial stream (orange and yellow vectors). Upon approaching the tank wall, the radial flow is separated into two streams one flowing towards the lower and the other towards the upper part of the tank. This results in the formation of two large scale circulation zones one above and one below the radial discharge stream as seen in Figure 4-1. These circulation zones, together with turbulence dispersion are the main reason for the mixing capability of the stirred tank. Since the impeller is positioned at T/3 from the tank bottom, the intensity of the lower circulation zone is significantly stronger than the upper circulation zone, indicating that more mixing takes place in this region. The locus of the upper circulation zone shifts closer to the impeller centre plane and nearer to the axis as the angular distance from the baffle decreases (c.f. Figure 4-1(a) and 4-1(b)). This has also been observed with reported experimental data (Costes and Cordec, 1988; Schafer et al., 1997).

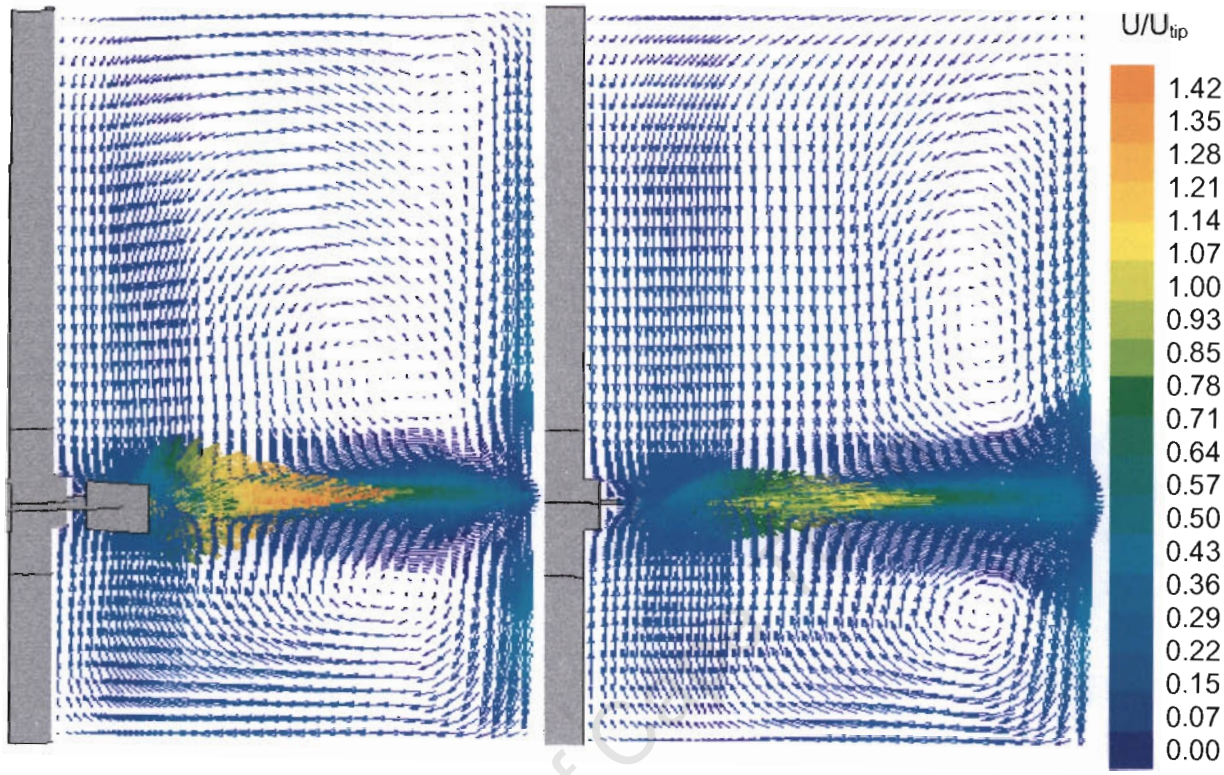

Figure 4-1: Mean Velocity vectors in the r-z plane at (a) 10 ° and (b) 45 ° before a baffle plane (Model = 230 000 control volumes, MRF, UD).

4.1.2. Turbulence Distribution

Figure 4-2 (a) shows contours of the predicted turbulent kinetic energy in the vertical plane midway between two baffles. The predicted contours show the expected high values of k concentrated in the region of the radial discharge stream of the impeller, with maximum values of about $0.055U_{tip}^2$. This value is close to the experimental value of $0.07U_{tip}^2$ reported by Schafer et al. (1997). The predicted results reveal very low turbulence levels in the bulk of the tank. Regions of local maximum k values in the impeller stream can be distinguished. These locally high values of k can be attributed to the trailing vortices produced by the preceding blade.

An additional perspective is obtained in the circumferential plane at the centre of the impeller shown in Figure 4-2 (b). A region of high k values can be identified behind each blade which extends to about 15° behind the trailing blade. This represents a good indication of the presence

and extent of trailing vortices detached from the edges of the impeller blades and convected by the impeller stream into the bulk of the tank. In the outer region, the vortices are no longer driven by the impeller and they collapse and disappear at a radial distance of about two blade widths. This distance is in agreement with the extent of the region where periodic flow is observed (Lee and Yianneskis, 1994).

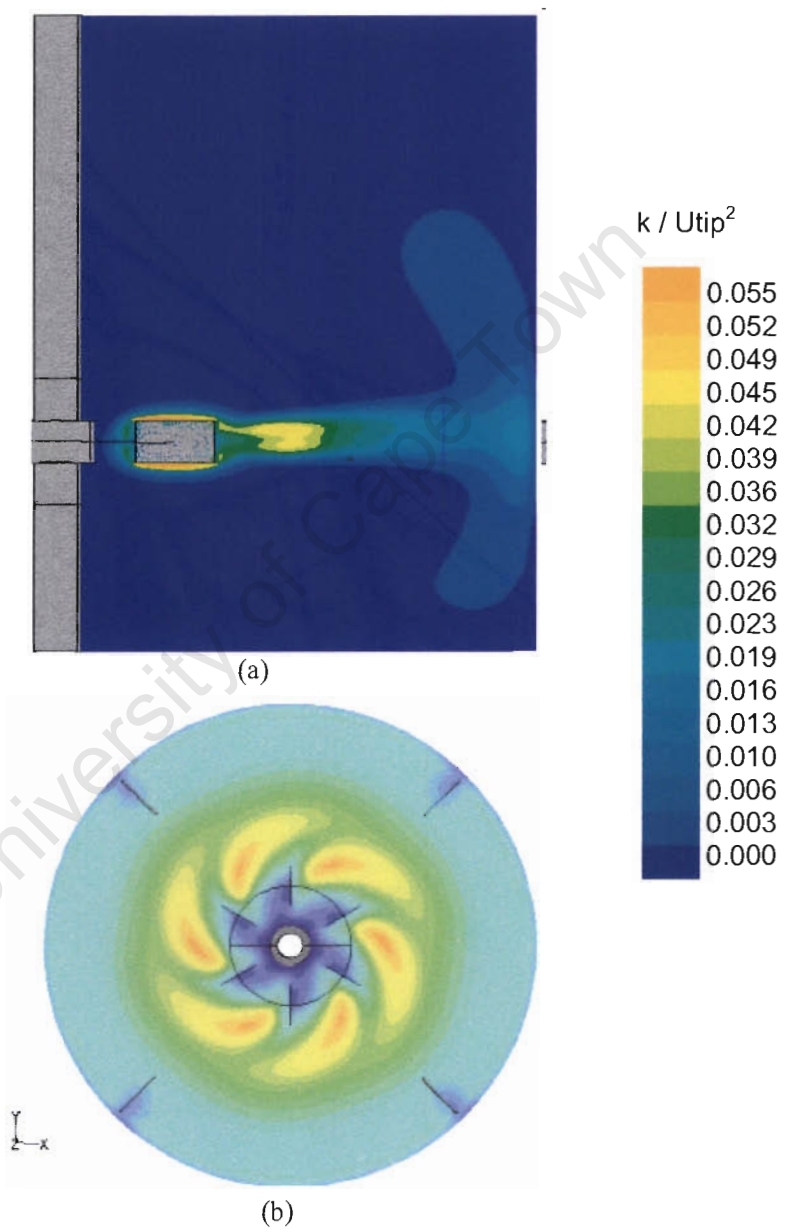

Figure 4-2: Turbulent kinetic energy contours, (a) mid-baffle plane and (b) impeller centre plane (Model = 230 000 control volumes, MRF , UD, standard k-ε).

4.1.3. Power Numbers

The Power numbers, N_p were calculated from the torque exerted on the impeller and shaft surfaces by the pressure and viscous forces of the fluid. In Figure 4-3, Power numbers computed over a range of Reynolds numbers are compared with experimental data of Rushton et al. (1950) on a log-log plot. The computed N_p with Re shows the typical power curve correlation and the values are in very good agreement with the empirical data of Rushton et al. (1950).

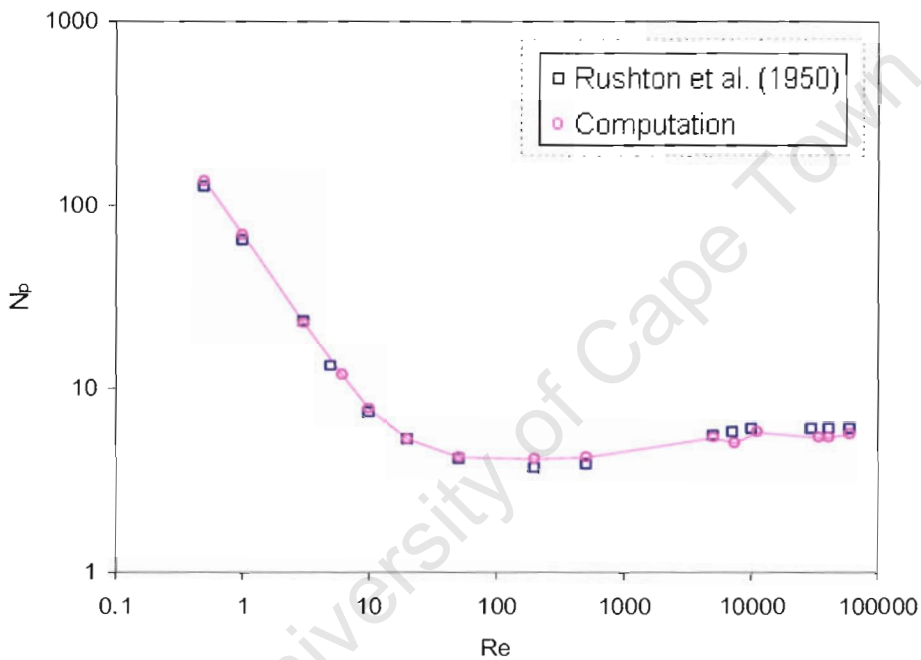

Figure 4-3: Variation of Power Numbers, N_p with Reynolds number, Re. (Model = UD scheme, MFR, standard-k-ε).

4.2. Effect of Grid Density on Predicted Flow Variables

An important flow phenomenon is the trailing vortex pair generated at the tips of the turbine blade, first identified by the pioneering work of Van't Riet and Smith (1974). These authors reported that the fluid within the vortex region experiences the highest energy dissipation rates within the mixing tank. For multi-phase flows, knowledge of the trailing vortex system is important for understanding the system power requirements, gas cavity generation and gas bubble break-up (Escudié et al., 2004). Therefore the numerical models employed should be able to

resolve this flow structure. In Figure 4-4, mean velocity vectors in the vicinity of an impeller blade simulated with three different grid densities investigated are shown.

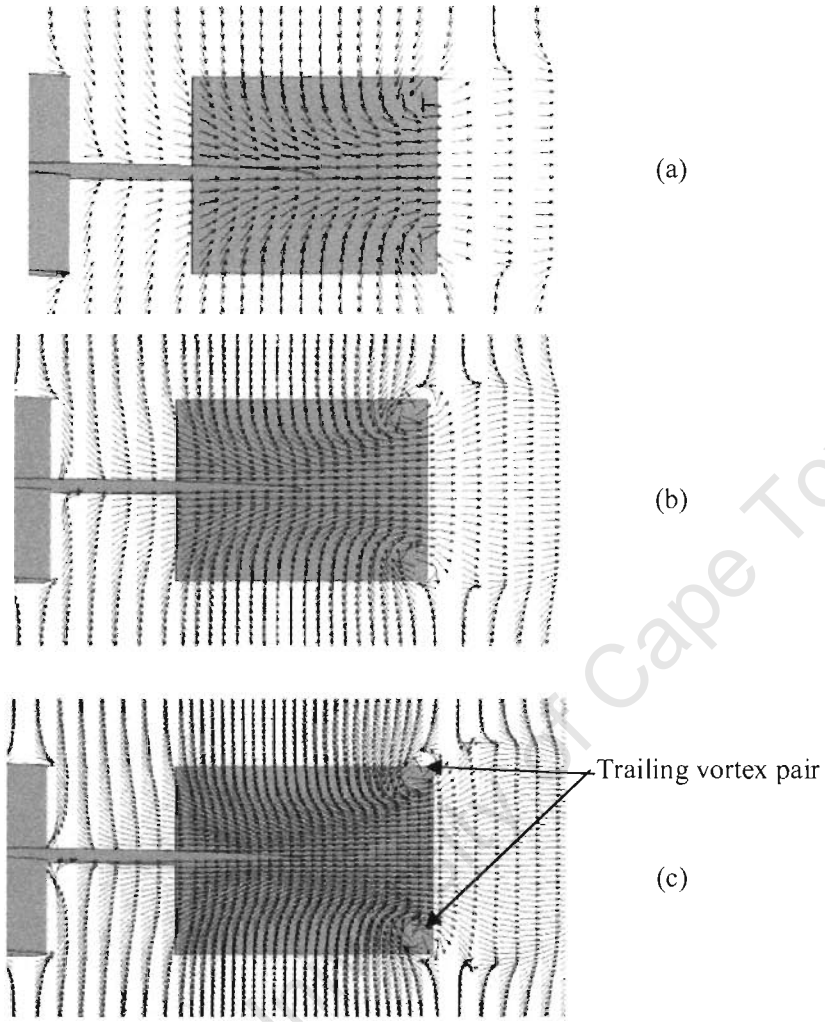

Figure 4-4: Trailing vortices at the tip of impeller blades, predicted by grid densities (a) 230 000, (b) 830 000 and (c) 1 900 000 control volumes. Vectors are not drawn to scale. (Model = UD scheme, MFR, standard-k-ε).

As can be seen, the trailing vortex pair is evident in the velocity field obtained with grids consisting of 830 000 and 1 900 000 control volumes. This phenomenon is not however resolved on the coarser grid with 230 000 control volumes. Therefore, it can be concluded that the ability of the CFD simulation to resolve important flow features such as the vortex structure near the impeller blades depends on the density of the numerical grid.

Table 4.1 compares Power numbers computed for the different grid densities investigated.

Table 4-1: Effect of grid density on predicted Power Numbers (Re = 40 000).

	N_P
Measured (Rushton et al. (1950))	6.069
Grid 1	4.166
Grid 2	4.694
Grid 3	4.953
Grid 4	5.067

It can be seen that the computed Power numbers are less than the experimentally determined value, although the discrepancy decreases with larger grid density with a difference of about 20 % between Power numbers obtained with the coarsest and finest grids. Rutherford et al. (1996) showed that Power numbers increase with decreasing blade thickness. However, even for the blades with smallest thickness considered, the measured Power numbers were lower than the values of Rushton et al. (1950) suggesting that the Power numbers of these authors may be too high.

For a more detailed assessment of effect of grid density on the predicted flow field, profiles of the mean velocity components and turbulent kinetic energy obtained with the different grid densities in Table 3-1 were compared with each other and with experimental data of Wu and Patterson (1989) for a fully turbulent Reynolds number of 40 000.The grid dependency study was conducted using the MRF impeller model with the standard k-ε turbulence model. In all cases, the convective terms were discretized using the first order upwind scheme.

Figures 4-5 and 4-6 presents axial profiles of the dimensionless mean velocity components and the turbulent kinetic energy k at three radial positions in a mid-baffle plane (c.f. Appendix B) obtained with the four grids. The results show that near the impeller tip (r/T = 0.185), the fluid experiences strong radial and tangential velocity components, with maximum values of approximately $0.7U_{tip}$ and $0.5U_{tip}$ respectively occurring at the impeller center plane (z/H ~ 0.3). Moving further from the impeller tip at r/T = 0.285 and r/T = 0.389, the tangential component of the mean velocity decreases, but the flow still maintains a strong radial component, hence resulting in the classification of the Rushton turbine as radial discharge flow impeller. As can be seen from Figure 4-6, the axial component of the mean velocity is almost negligible in the

impeller stream. With the exception of the coarse grid, the mean velocity components of the fluid computed with all grid densities are very similar if not identical at the three radial positions, suggesting that further grid refinement would have no effect on the predicted results.
Near the impeller tip, at r/T = 0.185, the good quantitative agreement with the measured values was achieved for all grids, except for the coarsest grid (Grid 1) which severely under-estimates the radial and tangential velocity components. This indicates that on this grid, the large spatial gradients in velocities occurring in the vicinity of the trailing vortices are poorly approximated by the discretization scheme. Further from the impeller tip, i.e. at r/T = 0.285 and r/T = 0.389, the numerical predictions slightly over-estimate the mean radial and tangential velocities in the vicinity of the impeller blades (i.e. z/H ~ 0.3 to z/H ~ 0.36). According to Jenne and Reuss (1999), the standard k-ε model over-estimates the turbulent shear stress and consequently this could lead to large estimates of mean radial and tangential velocities in the impeller stream as observed in the present study.

The predicted turbulence level in the impeller stream was examined by plotting values of the turbulent kinetic energy k at the three radial positions (c.f. Figure 4-6). Near the impeller tip at r/T = 0.185, the predicted results show two maximum values for k occurring at z/H ~ 0.31 and z/H ~ 0.35. These maximum k values can be attributed to the trailing vortices occurring one above and the other below the impeller center plane. The numerical results show maximum values of k at r/T = 0.285 and minimum values at r/T = 0.389 which is consistent with the experimental studies of Wu and Patterson (1989) who reported that near the impeller tip, the turbulence was still developing in the impeller stream, becoming dominant from r/T = 0.258 and decaying further from there.

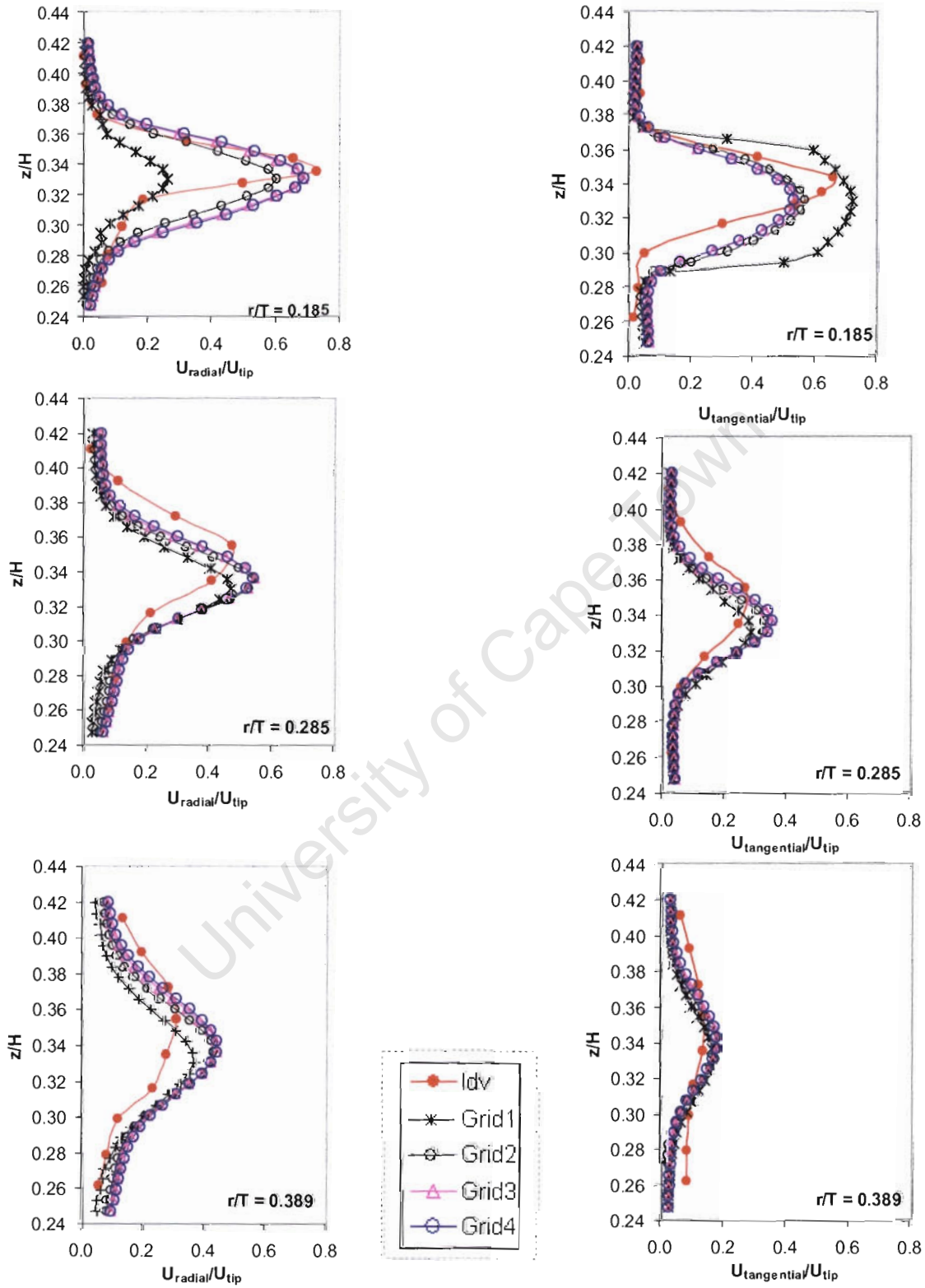

Figure 4-5: Effect of grid density on computed mean radial and tangential velocity components. (Model = UD scheme, MFR, standard-k-ε).

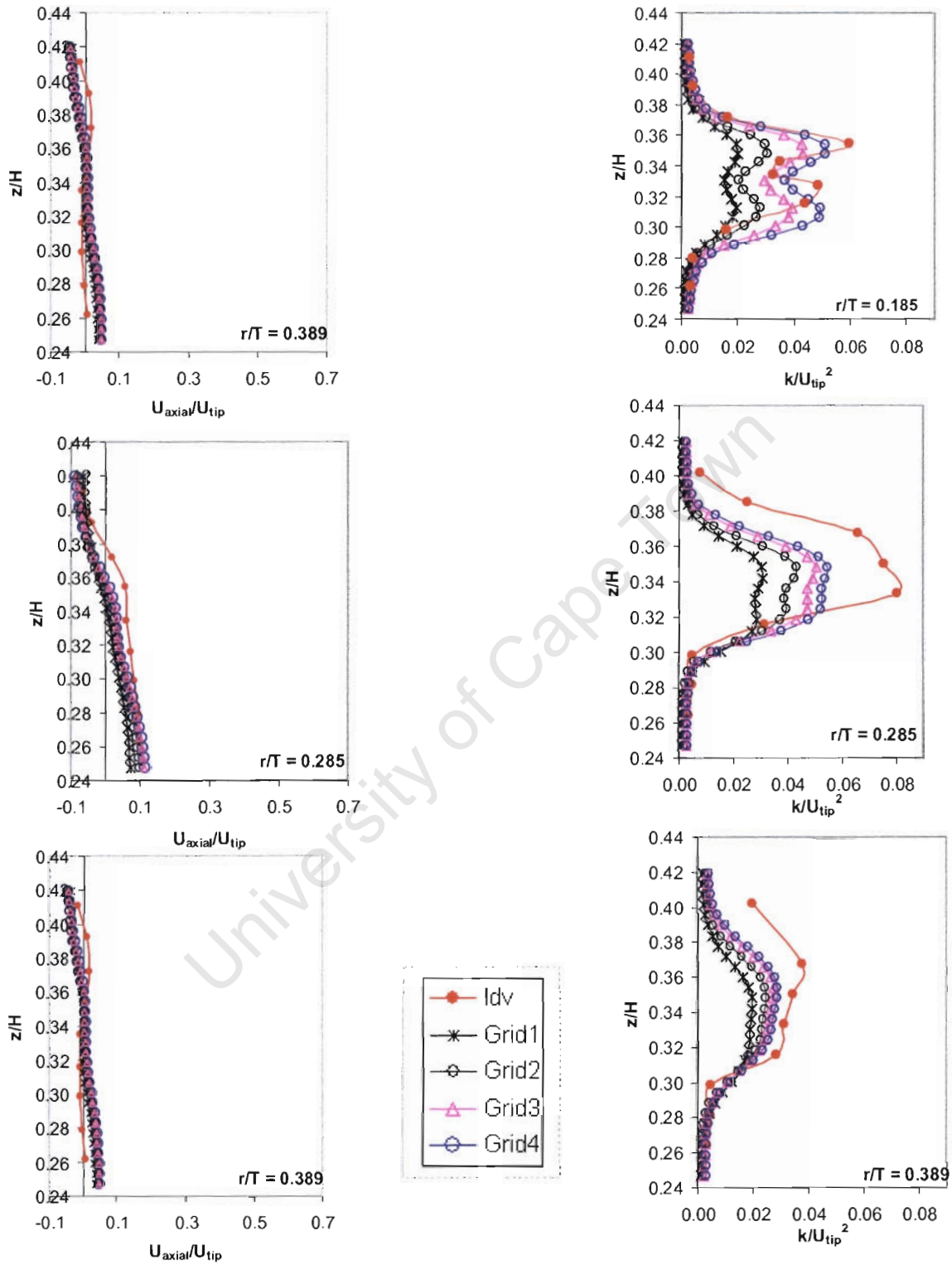

Figure 4-6: Effect of grid density on computed mean axial velocity and turbulent kinetic energy, k. (Model = UD scheme, MFR, standard-k-ε).

It can be seen that the grid density has more influence on the predicted turbulent kinetic energy values than on the predicted velocity field even though good qualitative agreement with LDV data has been achieved for both. This is especially so near the impeller tip where there is quite a significant difference between the predictions of the finer grids, Grid 3 and Grid 4. Further investigation is required to determine whether the discrepancies are due to numerical error in the first order upwind differencing scheme or due to inadequacies in the standard k-ε turbulence model and this is discussed in the next sections.

Other researchers using similar numerical techniques have also found that the numerical simulations severely under predicted turbulence levels in the impeller discharge flow of the stirred tank (Ranade et al., 1989 and 2002; Ng et al., 1998; Wechsler et al., 1999; Montante et al., 2001; Jaworski and Zakrzewska, 2002; Aubin et al., 2004). In most of these cases, the authors have attributed this discrepancy to the assumption of locally isotropic turbulence in the k-ε turbulence model. However, studies of Jaworski and Zakrzewska found no improvement in the predicted k values when the non-isotropic RSM model was used. Furthermore, Wu et al. (1989) found that measured RMS turbulent velocity values with which the present simulations are compared were very similar in the radial, axial and circumferential directions. Therefore the assumption of isotropic turbulence was acceptable. This suggests that the generally observed discrepancy in the predicted k values is not only dependent on the isotropic assumption of the k-ε turbulence model.

4.3. Effect of Discretization Scheme

The effect of various discretization schemes on the predicted flow in the impeller stream was investigated by conducting simulations with the Central and QUICK discretization schemes. Power numbers calculated from the Central and QUICK discretization schemes were both higher than the value obtained using the upwind discretization scheme (c.f. Table 4-2) and are thus closer to the measured value of Rushton et al (1950).

Table 4-2: Effect of discretization scheme and impeller model on predicted Power Numbers (Re = 40 000).

	N_P
Measured (Rushton et al (1950))	6.069
Grid 4 (Upwind Differencing)	5.067
Grid 4 (Central Differencing)	5.314
Grid 4 (QUICK)	5.398
Grid Sliding Mesh	5.536

The effect of various discretization schemes on the computed velocity and turbulent kinetic energy in the impeller stream are shown in Figure 4-7. In all cases the MRF model was used and simulations were performed on the fine grid, Grid 4. It can be seen that the choice of discretization scheme significantly influences the predicted turbulent kinetic energy levels. The k values obtained with the central and QUICK differencing schemes are almost identical and show good agreement with the experimental data. This is an important result as it suggests that the generally reported underestimation of turbulence levels may have been caused by numerical errors in the simulations, rather than inadequacies in the turbulence model as suggested by most researchers. The k values obtained with the upwind scheme substantially differ from the other two schemes suggesting that this scheme may not be acceptable for the simulation of turbulent flow in stirred tanks. Mean radial and tangential velocity profiles at r/T = 0.285 obtained with the upwind, central and QUICK discretization schemes are very similar. Therefore, considering the robustness of the iteration process the QUICK scheme was chosen as the optimal scheme and employed for the rest of the simulations.

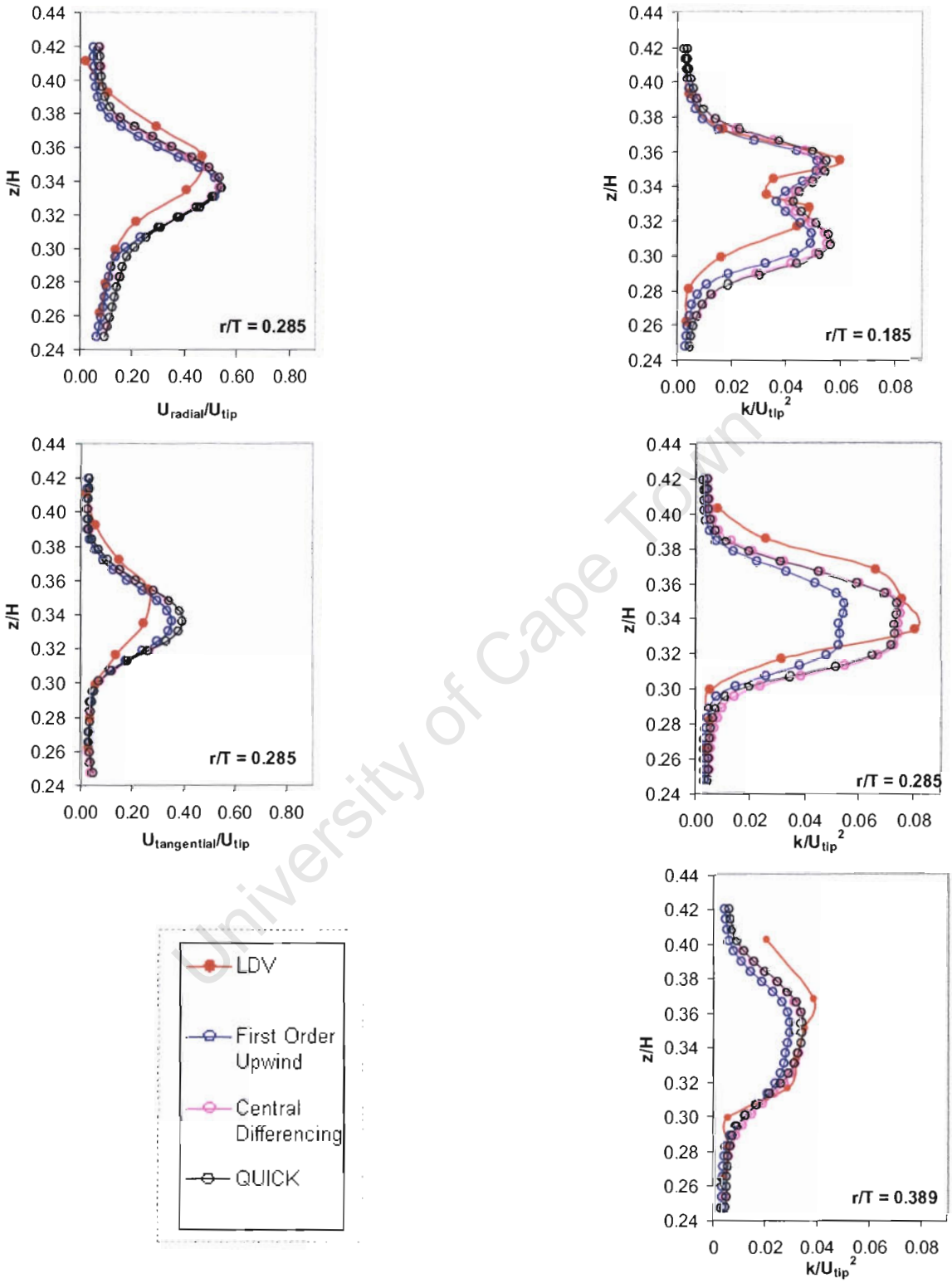

Figure 4-7: Effect of discretization scheme on computed mean velocity components and turbulent kinetic energy, k. (Model = Grid 4, MFR, standard-k-ε).

4.4. Comparison of Impeller Modeling Approach

The time-dependent SM impeller model predicted a Power number of 5.536 for a Reynolds number of 40 000, which is closer to the experimental value than the value calculated with the MFR approach (c.f. Table 4.2). In Figure 4-8, the velocity and turbulent kinetic energy profiles computed with the SM and MRF impeller models are compared. The mean velocity components and the turbulent kinetic energy at r/T = 0.285 are shown. On the fine grid, the mean velocity profiles calculated with the SM and MRF models are almost identical, except in the region of the impeller blade where the SM calculations are lower and thus show better agreement with the experimental data. The turbulent kinetic energy levels calculated with the two impeller models are also similar and show good agreement with the experimental data.

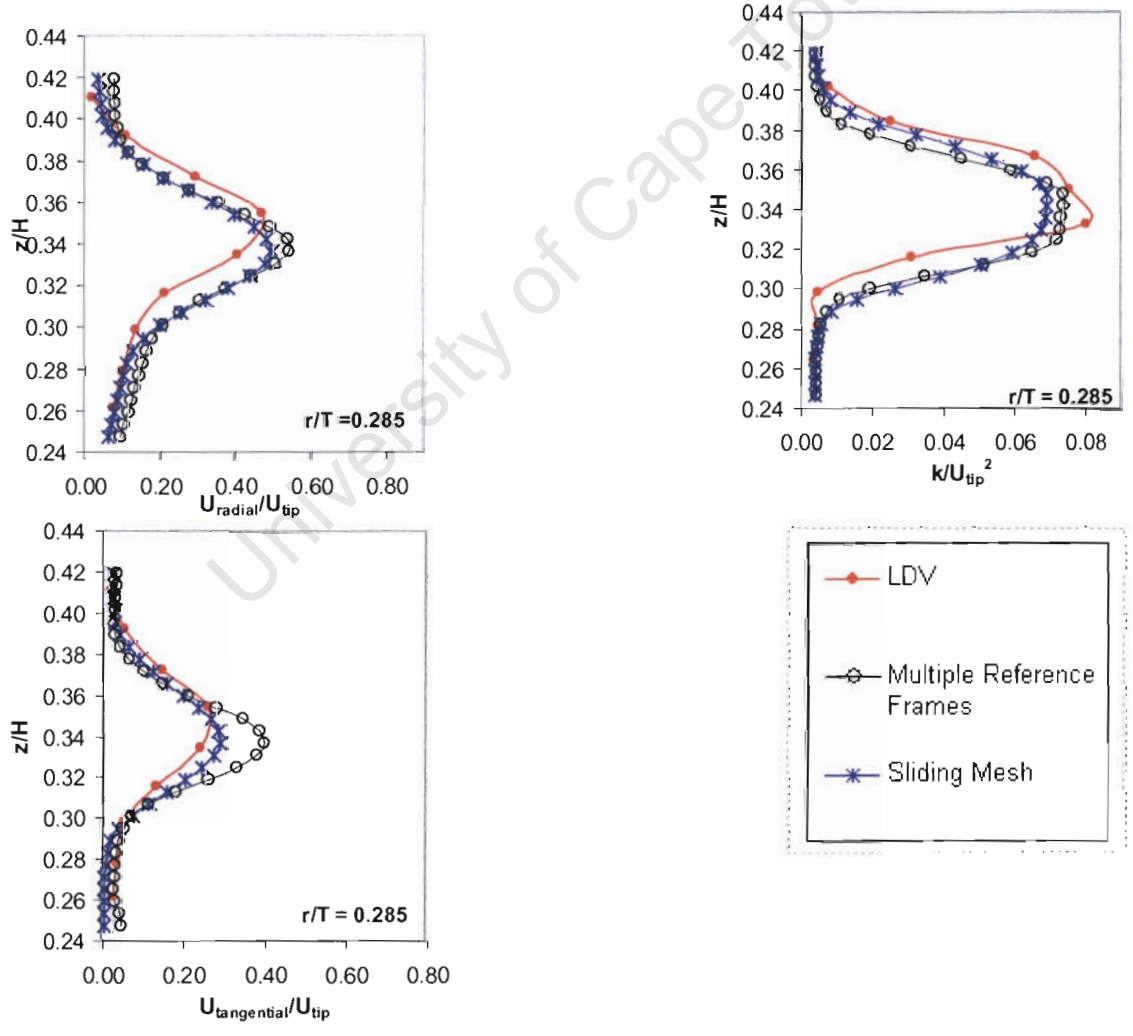

Figure 4-8: Effect of impeller model on computed mean velocity and turbulent kinetic energy, k.

4.5. Comparison of Turbulence Models

The effect of the applied turbulence model on the predicted flow field was limited to the standard k-ε and the RNG k-ε models. Axial profiles of the dimensionless axial and tangential mean velocity components and the turbulent kinetic energy at the radial distance r/T = 0.285, are shown in Figure 4-9, together with the LDV data of Wu and Patterson (1989).

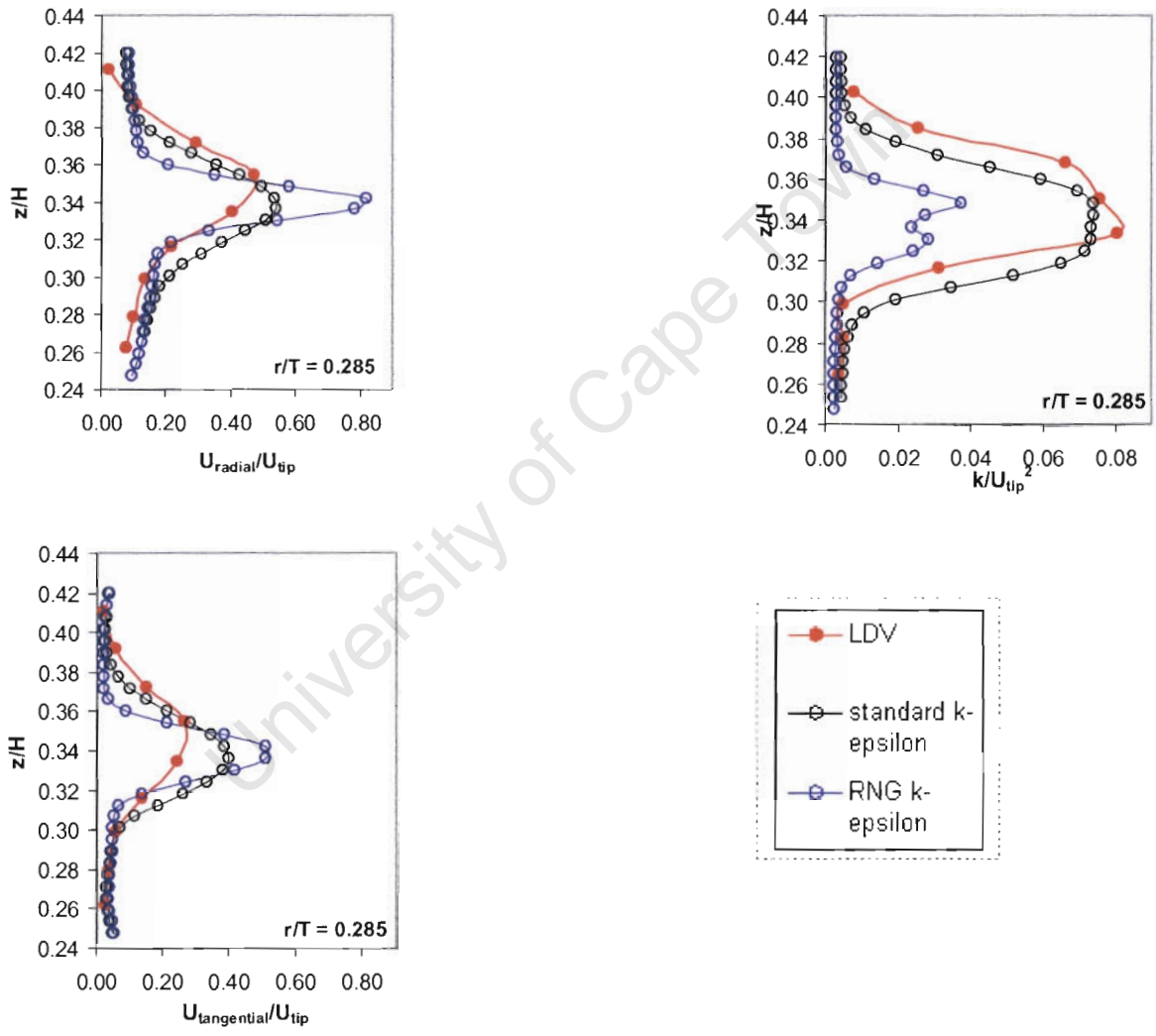

Figure 4-9: Effect of turbulence model on computed mean velocity and turbulent kinetic energy.

The predicted mean velocities for the two turbulence models are similar except at the impeller centre plane where both the mean tangential and radial velocity values of the RNG k-ε model are significantly higher than both the standard k-ε predictions and the experimental data.
This result is in agreement with previous findings of Jenne and Reuss (1999) who suggested that the high velocity values predicted by the RNG k-ε model were induced by the formulation of the model that generally underestimates the energy loss in the outflow of the impeller. This argument seems to be supported by the predicted turbulent kinetic energy profile which still exhibits two local maxima due to the trailing vortices at this radial position. The RNG k-ε model underestimates the turbulent kinetic energy levels in the impeller stream. Contrary to previous studies by Jaworski and Zakrzewska (2002) and Aubin et al. (2004), the present study shows significant differences between the predicted k values using the standard- k-ε and the RNG k-ε turbulence models. In the present study, the standard k-ε model shows good correlation with experimental data, which was not observed in the mentioned studies. The differences in the CFD results may be attributed to the high grid density used in the present study and the discretization schemes.

CHAPTER 5 CONCLUSIONS

The aim of this thesis was to present an accurate CFD approach that models the hydrodynamic properties of flow in stirred tanks. The effect of the grid resolution and choice of discretization scheme on the predicted single-phase flow has been investigated. A comparison of the steady state MRF and time-dependent SM impeller models was made. An attempt was made to compare isotropic and non-isotropic turbulence models. However, a converged solution for the non-isotropic Reynolds stress model (RSM) was not achieved, limiting the study to two variants of the isotropic k-ε model. In this Chapter, the conclusions regarding the findings of the study are presented.

5.1. Numerical Grid Requirements

From the grid dependency study using a first order discretization scheme and grids consisting of 33 000, 230 000, 830 000 and 1 900 000 control volumes, the following conclusions can be drawn:

- In order to resolve the trailing vortex structures behind the impeller blade, grid resolutions of more than 192 control volumes covering the blade surface were required. This was achieved on the grids consisting of 830 000 and 1 900 000 control volumes. On the other two grids, the vortex structures were not resolved.
- The computed Power numbers in the laminar Reynolds number range were in reasonable agreement with experimental data. In the turbulent Reynolds number range, the Power numbers calculated with all grids were lower than the experimental data from the literature. However, the discrepancy between computed values and experimental data was reduced with finer grids.
- The numerical grid consisting of 33 000 control volumes predicts profiles of the velocity components and turbulent kinetic energy in the impeller stream that show substantial deviation from the experimental data. Velocity components computed with grids consisting of 230 000, 830 000 and 1900 000 control volumes are similar if not identical.
- Significantly finer grids are required in order to attain grid independence for turbulent kinetic energy than for the mean velocities.

5.2. Discretization schemes

Simulations were performed on the fine grid consisting of 1900 000 control volumes using the first order upwind and higher order central and QUICK discretization schemes.

- The higher order central and QUICK discretization schemes predicted Power numbers that were in better agreement with the experimental data. The computed Power numbers were lower than the experimental data of Rushton et al. (1950) by 17%, 12% and 11% for the upwind, central and QUICK discretization scheme respectively.
- The discretization scheme was found to significantly influence the computed turbulent kinetic energy in the impeller stream. The central and QUICK discretization schemes predicted turbulent kinetic energy values that are in good agreement with the experimental data and the upwind differencing scheme was found to significantly underestimate the experimental data. This is an important finding as it suggests that the general under-prediction of turbulence reported in the literature is caused by numerical errors, rather than inadequacies in the k-ε turbulence model as suggested by many researchers.
- The choice of discretization scheme was found to have no substantial effect on the predicted mean velocity values in the impeller discharge stream of the stirred tank.

5.3. Impeller Models

The choice of impeller modeling approach, Multiple Reference Frames (MRF) or Sliding Mesh (SM) model, was found to have no significant effect on the predicted mean velocity. Both the MRF and SM models predicted turbulent kinetic energy levels that are in good agreement with the experimental data. The Power number obtained with the SM model was lower than the experimental value by about 8% as compared to 11% for the value obtained with the MRF model.

5.4. Turbulence Models

Generally, the predicted mean velocities obtained with the standard form of the k-ε model showed better agreement with the experimental data than the predictions using the RNG k-ε turbulence

model. The RNG k-ε model was found to significantly under-estimate the turbulent kinetic energy levels in the impeller discharge stream, while the standard models showed good agreement with the experimental data.

From the various possible combinations concerning grid resolution, discretization schemes, impeller modeling methods and choice of turbulence models, a reasonably accurate CFD method has been presented for the simulation of single-phase turbulent flow in stirred tanks. In order to isolate numerical errors from the predicted flow, very fine grids compared to what has been reported in many previous studies in the literature were used. It was also necessary to use a higher order discretization scheme on adequately as flow predictions using a first order scheme were unsatisfactory. Furthermore, the good agreement between predicted and experimental turbulence levels obtained in the present study seems to suggest that numerical error caused by insufficient grid densities or inadequate discretization schemes is the main reason for the generally reported under-prediction of turbulence in the impeller stream of the stirred tank. The steady-state MFR impeller model gave similar results as the time-dependent SM model. Therefore, the extra computational expense needed for the transient calculation was not justified. From the good agreement achieved between the CFD results and experimental observations for the mean flow velocities as well as the turbulence levels, it can be concluded that this method can be extended to the simulation of the more complex multi-phase flow. However, because of the many variables involved in determining the accuracy of a CFD simulation, the prudent extension to multi-phase flow processes should be accompanied by further numerical experiments and careful validation with measured data.

REFERENCES

1. Aubin, J., Fletcher, D.F. & Xuereb, C., 2004. Modeling Turbulent Flow in stirred tanks with CFD: the Influence of the Modeling Approach, Turbulence model and Numerical Scheme. *Experimental Thermal and Fluid Science,* 28: 431-445.

2. Aubin, J., Le Sauze, N., Bertrand, J., Fletcher, D.F. & Xuereb, C., 2004. PIV measurements of flow in an aerated tank stirred by a down- and up-pumping axial flow impeller. *Experimental Thermal and Fluid Science,* 28: 447-456.

3. Abujelala, M.T. & Lilley, D.G., 1984. Limitations and Empirical Extensions of the k-ε Model as Applied to Turbulent Confined Swirling Flows. *Chemical Engineering Communications*, 31:223-236.

4. Bakker, A., 1992. Hydrodynamics of Stirred Gas-Liquid Dispersions. *Ph.D. Thesis*, *Delft University of Technology*, *the Netherlands*.

5. Bakker, A., LaRoche, R.D., Wang, M. & Calabrese, R.V., 2000. Sliding Mesh Simulation of Laminar Flow in Stirred Reactors. *The Online CFM Book, 1998* Available 23 August 2003 < http: //www.bakker.org/cfm.>.

6. Bartels, C., Breuer, M., Wechsler, k. & Durst, F., 2002. Computational Fluid Dynamics Applications on Parallel-Vector Computers: Computations of Stirred Vessel Flows. *Computers and Fluids*, 31(1): 69-97.

7. Brucato, A., Ciofalo, M., Grisafi, F. & Micale, G., 1998. Numerical Prediction of Flows in Baffled Stirred Vessels: A Comparison of Alternative Modeling Approaches. *Chemical Engineering Science*, 53(21):3653-3684.

8. Campolo, M., Sbrizzai, F. & Soldati, A., 2003. Time-dependent Flow Structure and Lagrangian Mixing in Rushton Impeller Baffled-tank Reactor. *Chemical Engineering Science*, 58: 1615-1629.

9. Converti, A., Del Borghi, M., Ferraiolo, G. & Sommania, C., 1996. Mechanical Mixing and Biological Deactivation: The Role of Shear Stress Application Time. *The Chemical Engineering Journal*, 62: 155-167.

10. Costes, J., & Courdec, J.P., 1988. Study by Laser Doppler Anemometry of the Turbulent Flow Induced by a Rushton Turbine in a Stirred Tank: Influence of Size of Units-I. Mean Flow and Turbulence. *Chemical Engineering Science*, 43:2751-2764.

11. Deglon, D.A., 1998. A Hydrodynamic Investigation of Fine Particle Flotation in a Batch Flotation Cell. *Ph.D. Thesis, University of Cape Town*.

12. Deshpande, V.R, & Ranade, V.V., 2003. Simulation of Flows in Stirred Vessels Agitated by Dual Rushton Impellers using Computational Snapshot Approach. *Chemical Engineering Communications*, 190: 236-253.

13. Derksen J.J. & Van Den Akker, H.E.A, 1999. Large Eddy Simulations on the Flow Driven by a Rushton Turbine, *AICHE Journal*, 45: 209-221.

14. Dyster, K. N., Kousakos, E., Jaworski, Z. & Nienow, A.W., 1993. An LDA Study of the Radial Discharge Velocities Generated by a Rushton Turbine: Newtonian Fluids, Re $\geq$ 5. *Trans IChemE, Part A*, 71: 11-23.

15. Eggels J.M.G., 1996. Direct and Large Eddy Simulations of the Turbulent Fluid Flow using the Lattice-Boltzman Scheme, *International Journal of Heat and Fluid Flow*, 17: 307-323.

16. Escudié, R., Bouyer, D. & Liné, A., 2004. Characterization of Trailing Vortices Generated by a Rushton Turbine. *AIChE Journal*, 50(1):75-86.

17. Ferziger, J.H. & Peric, M., 1997. Computational Methods for Fluid Dynamics. Berlin: Springer.

18. Fields S.D & Ottino, J.M., 1987. Effect of Segregation on the Course of Un-premixed Polymerization. *AIChE Journal*, 33: 959.

19. Fluent 6.1. User's Guide, 2003. *Fluent Inc*.

20. Fokema, M. D., Kresta, S.M., 1994. Importance of Using the Correct Impeller Boundary Conditions for CFD Simulations of Stirred Tanks. *The Canadian Journal of Chemical Engineering*, 72: 177-183.

21. Gosman, A.D., Lekakou, C., Politis, S. Issa, R.I & Looney, M.K., 1992. Multidimensional Modeling of Turbulent Two-Phase Flows in Stirred Vessels. *AIChE Journal*, 38(12):1946

22. Han, T., Humphrey, J.A.C. & Lauder, B.E., 1981. A Comparison of Hybrid and Quadratic-Upstream Differencing in High Reynolds Number Elliptic Flows, *Computer Methods in Applied Mechanics and Engineering*, 29:81-95.

23. Hartman, H., Derksen J.J., Montavon, C., Pearson, J., Hamill, I. S. & Van den Akker, H.E.A., 2004. Assessment of Large eddy and RANS stirred tank simulations by means of LDA. *Chemical Engineering Science*, 59: 2419-2432.

24. Harvey III, A.D. & Lee, C.K., 1995. Steady-State Modeling and Experimental Measurement of a Baffled Impeller Stirred Tank. *AIChE Journal*, 41:2177-2186.

25. Harvey III, A.D. & Rogers, S.E., 1996. Steady and Unsteady Computations of Impeller-Stirred Reactors. *AIChE Journal*, 42: 2701-2712.

26. Jaworski, Z. & Zakrzewska, B., 2002. Modeling of the Turbulent Wall Jet Generated by a Pitched Blade Turbine Impeller: The Effect of Turbulence Model. *Trans IChemE*, 80:846-854.

27. Jenne, M. & Reuss, M., 1999. A critical assessment on the use of k-ε turbulence models for simulation of the turbulent liquid flow induced by a Rushton-turbine in a baffled stirred-tank reactor. *Chemical Engineering Science*, 54: 3921-3941.

28. Kresta S.M. & Wood, P.E., 1991. Prediction of the Three-Dimensional Turbulent Flow in Stirred Tanks. *AIChE Journal*, 37(3):448

29. Lane, G.L., Schwarz, M.P. & Evans, G.M., 2002. Predicting Gas-Liquid Flow in a Mechanically Stirred Tank. *Applied Mathematical Modeling*, 26: 223-235.

30. Lauder, B.E. & Spalding, D.B., 1974. The Numerical Computation of Turbulent Flows. *Computer Methods in Applied Mechanics and Engineering*, 3: 269-289.

31. Lee, K.C. & Yianneskis, M., 1998. Turbulence Properties of the Impeller Stream of a Rushton Turbine. *AIChE Journal*, 44: 13-24.

32. Lee, K.C. & Yianneskis, M., 1994. The Extent of Periodicity of the Flow in Vessels Stirred by Rushton Impellers. *AIChE Symposium Series*, 90: 5-18.

33. Luo, J.Y., Gosman, A.D., Issa, R.I., Middleton, J.C. & Fitzgerald, M.K., 1993. Full Flow Field Computation of Mixing in Baffled Stirred Vessels, *Trans IChemE*, 71:342-344.

34. Marshall, E.M. & Bakker, A., 2003, Computational Fluid Mixing. USA: Fluent Inc.

35. Mavros, P., 2001. Flow Visualization in Stirred Vessels: A Review of Experimental Techniques, *Trans IChemE*, 79:113-127.

36. Mavros, P., Xuereb, C. & Bertrand, J., 1996. Determination of 3-D Flow Fields in Agitated Vessels by Laser-Doppler Velocimetry: Effect of Impeller Type and Liquid Viscosity on Liquid Flow Patterns. *Trans IChemE, Part A*, 74: 658-668.

37. Montante, G., Lee, K.C., Brucato, A. & Yianneskis, M., 2001. Numerical Simulations of the Dependency of Flow Pattern on Impeller Clearance in Stirred Vessels. *Chemical Engineering Science*, 56: 3751-3770.

38. Morud, K.E. & Hjertager, B.H., 1996. LDA Measurements and CFD Modeling of Gas-Liquid Flow in a Stirred Vessel. *Chemical Engineering Science*, 51: 233-249.

39. Ng, K. & Yianneskis, M., 2000. Observations on the Distribution of Energy Dissipation in Stirred Vessels. *Trans IChemE, Part A*, 78: 334-341.

40. Ng, K., Fentiman, N.J., Lee, K.C. & Yianneskis, M., 1998. Assessment of Sliding Mesh CFD Predictions and LDA Measurements of the Flow in A Tank Stirred by a Rushton Turbine, *Trans IChemE*, 76: 737-747.

41. Patankar, S.V., 1980. Numerical Heat Transfer and Fluid Flow. Hemisphere, Taylor & Francis Group, New York.

42. Ranade, V.V. & Van Den Akker, H. E. A., 1994. A Computational Snapshot of Gas-Liquid Flow in Baffled Stirred Reactors. *Chemical Engineering Science*, 49:5175-5192.

43. Ranade, V.V., 1997. An Efficient Computational Model for Simulating Flow in Stirred Vessels: a Case of Rushton Turbine. *Chemical engineering Science*, 52: 4473-4484.

44. Ranade V.V., Joshi, J.B. & Marathe, A.G., 1989. Flow Generated by Pitched Blade Turbines II: Simulation using k-ε Model. *Chemical Engineering Communications*, 81: 225-248.

45. Ranade, V.V., Tayalia, Y. & Krishnan, H., 2002. CFD Predictions of Flow near Impeller Blades in Baffled Stirred Vessels: Assessment of Computational Snapshot Approach. *Chemical Engineering Communications*, 189:895-922.

46. Rushton, J.H., Costich E.W. & Everett, H.J., 1950. Power Characteristics of Mixing Impellers –Part II. *Chemical Engineering Progress*, 46:467-476.

47. Rutherford, K., Mahmoudi, S.M. Lee, K.S. & Yianneskis, M., 1996. The Influence of Rushton Impeller blade and disc thickness on the mixing characteristics of Stirred Vessels. *Trans IChemE*, 74:369-378.

48. Schäfer, M.., Höfken, M. & Durst, F., 1997. Detailed LDV Measurements for Visualization of the Flow Field Within a Stirred-tank Reactor Equipped with a Rushton Turbine. *Trans IChemE, Part A*, 75: 729-736.

49. Tatterson, G. B., 1991, Fluid Mixing and Gas Dispersion in Agitated Tanks. McGraw-Hill Inc.

50. Tabor, G., Gosman, A.D. & Issa, R.I., 1996. Numerical Simulation of Flow in a Mixing Vessel Stirred by a Rushton Turbine, *Fluid Mixing V, IChemE Symposium Series,* 140: 25-34.

51. Van't Riet, K. & Smith, J.M., 1975. The Trailing Vortex System Produced by Rushton Turbine Agitators. *Chemical Engineering Science*, 30:1093-1105.

52. Versteeg, H.K. & Malasekara, W., 1995. An Introduction to Computational Fluids Dynamics: The Finite Volume Methods. England: Longman Scientific and Technical.

53. Wechsler, K., Breuer, M. & Durst, F., 1999. Steady and Unsteady Computations of Turbulent Flows Induced by a 4/45° Pitched-Blade Impeller. *ASME Journal of Fluids Engineering*, 121:318-328.

54. Wernerson E.S. & Tragardh, C., 1999. Scale-up of Rushton Turbine-Agitated Tanks. *Chemical Engineering Science*, 54:4245-4256.

55. White, F.M., 1991. Viscous Fluid Flow, McGraw-Hill International Editions.

56. Wu H. & Patterson, G.K, 1989a. Laser-Doppler Measurements of Turbulent-Flow Parameters in a Stirred Mixer. *Chemical Engineering Science*, 44:2207-2221.

57. Wu H., Patterson, G.K. & Van Doorn, M., 1989b. Distribution of turbulence energy dissipation rates in a Rushton turbine stirred mixer. *Experiments in Fluids*, 8:153-160.

58. Yianneskis, M., Popiolek, Z. & Whitelaw, J.H., 1987. An Experimental Study of the Steady and Unsteady Flow Characteristics of Stirred Reactors. *J. Fluid Mech.*, 175: 537-555.

APPENDIX A

Power Number Calculation

Table A-1: Predicted Power numbers presented in tabular form

		Numerical Results			Experimental
Re	N	Torque (Nm)	Power (Nm/s)	N_p	N_p
0.5	0.0031	6.4571E-08	0.00	133.39	122.90
1.0	0.0061	1.3024E-07	0.00	67.27	63.03
3.0	0.0184	3.9564E-07	0.00	22.70	22.88
6.0	0.0367	8.2081E-07	0.00	11.78	13.18
10.0	0.0612	1.4879E-06	0.00	7.68	7.33
20.0	0.1224	4.0501E-06	0.00	5.23	5.25
50.0	0.3061	2.0120E-05	0.00	4.16	4.12
200.0	1.2243	3.1722E-04	0.00	4.10	3.68
500.0	3.0606	2.0560E-03	0.04	4.25	3.88
5000.0	30.6064	2.6257E-01	50.49	5.42	5.48
7300.0	44.6853	5.1391E-01	144.29	4.98	5.77
11358.5	5.1667	5.5433E-03	0.18	5.70	6.00
33709.0	15.3333	4.6298E-02	4.46	5.40	6.07
40000.0	244.8508	1.6719E+01	25721.67	5.40	6.07
60000.0	367.2762	3.9224E+01	90516.79	5.63	6.07

APPENDIX B

Figure B-1: Positions at which flow data was sampled

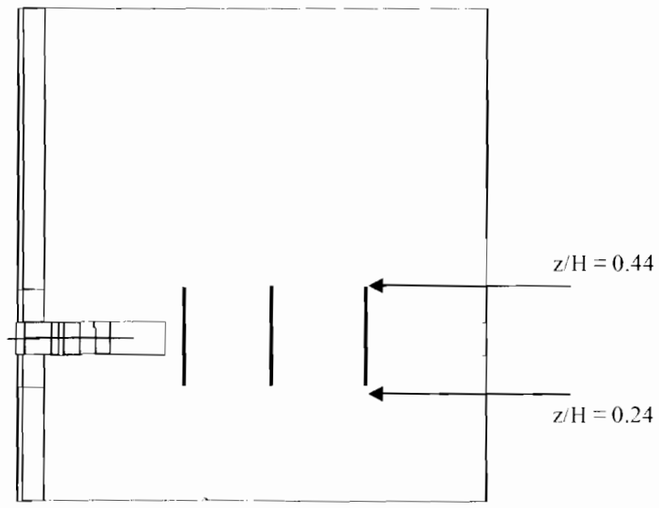

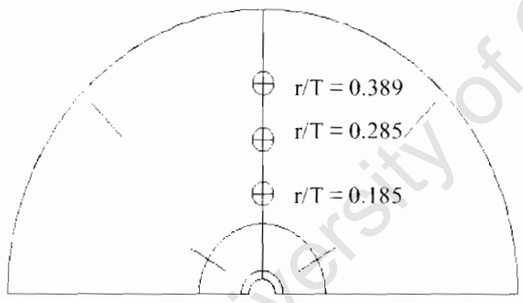

APPENDIX C

Predicted velocity components and turbulent kinetic energy presented in tabular form

Table C-1: Radial Velocity at r/T = 0.185

	r/T = 0.185 Radial Velocity (m/s)						
z/H	**Upwind**	**Upwind**	**Upwind**	**Upwind**	**Central**	**QUICK**	**RNG**
	GRID 1	GRID 2	GRID3	GRID 4	GRID 4	GRID 4	GRID 4
0.4194	0.1322	0.5861	0.6328	0.5738	1.1723	1.1857	1.5794
0.4135	0.143	0.6514	0.6882	0.6344	1.3108	1.3234	1.6823
0.4076	0.1576	0.7252	0.7738	0.7323	1.4935	1.4985	1.7895
0.4016	0.1801	0.8246	0.9016	0.8821	1.7492	1.7433	1.9218
0.3957	0.2211	0.9691	1.0944	1.1086	2.1171	2.0995	2.1183
0.3898	0.3249	1.1989	1.3934	1.458	2.6628	2.6338	2.4439
0.3838	0.5579	1.5807	1.8745	2.0157	3.4982	3.4621	2.9975
0.3779	0.9765	2.2254	2.7085	2.9493	4.8097	4.7758	3.9268
0.3719	1.9933	3.4618	4.2358	4.616	6.8858	6.9022	5.472
0.3660	2.3041	5.5847	7.0068	7.6061	10.128	10.295	8.0734
0.3601	2.7902	8.4231	11.414	12.172	14.419	14.798	11.709
0.3541	4.439	12.424	15.953	16.694	18.445	18.729	15.325
0.3482	6.3252	16.221	19.891	20.544	21.696	21.869	18.91
0.3422	8.0965	19.638	23.208	23.701	24.131	24.305	22.236
0.3363	9.5882	22.256	25.58	25.87	25.68	25.812	24.778
0.3304	10.152	23.276	26.393	26.552	26.158	26.217	25.617
0.3244	9.5976	22.283	25.328	25.546	25.523	25.551	24.595
0.3185	8.3906	19.776	22.946	23.316	23.956	23.959	22.53
0.3125	6.6843	16.703	19.936	20.455	21.737	21.722	20.049
0.3066	4.8432	13.318	16.632	17.256	19.053	19.064	17.391
0.3007	3.1972	9.8141	13.052	13.714	15.739	15.986	14.536
0.2947	2.052	6.6033	8.9585	9.5633	11.724	12.051	11.122
0.2888	2.2134	4.5521	5.8387	6.2663	8.1315	8.3135	7.9343
0.2829	1.4384	3.0401	3.9502	4.2472	5.7144	5.8224	5.8517
0.2769	0.7297	2.1743	2.852	3.0575	4.1812	4.2855	4.5686
0.2710	0.3367	1.6259	2.1811	2.3116	3.1785	3.3106	3.7103
0.2650	0.1671	1.265	1.7192	1.7999	2.4861	2.6498	3.0615
0.2591	0.0469	0.9839	1.3631	1.4117	1.9706	2.1585	2.522
0.2532	-0.0407	0.7554	1.0652	1.0949	1.5618	1.7643	2.0718
0.2472	-0.105	0.5641	0.8195	0.8406	1.23	1.4383	1.7341

Table C-2: Tangential Velocity at r/T = 0.185

	r/T = 0.185 Tangential Velocity (m/s)						
z/H	**Upwind**	**Upwind**	**Upwind**	**Upwind**	**Central**	**QUICK**	**RNG**
	GRID 1	GRID 2	GRID3	GRID 4	GRID 4	GRID 4	GRID 4
0.4194	0.9724	1.1105	0.9174	0.9932	1.6165	1.6413	2.0488
0.4135	0.9055	1.0741	0.8619	0.9481	1.5799	1.5935	1.8434
0.4076	0.8171	0.998	0.7631	0.862	1.5184	1.5191	1.5834
0.4016	0.7121	0.916	0.6745	0.7931	1.5023	1.491	1.3825
0.3957	0.5969	0.8471	0.6238	0.7724	1.5802	1.5595	1.298
0.3898	0.4863	0.8054	0.6322	0.8255	1.8012	1.7744	1.3644
0.3838	0.4651	0.8175	0.7367	0.9973	2.2392	2.2114	1.6179
0.3779	0.6175	0.9656	1.0513	1.4033	3.0297	3.0089	2.1204
0.3719	1.6674	1.6511	1.8983	2.3487	4.4085	4.3903	3.0203
0.3660	12.133	3.5813	4.0718	4.5106	6.6201	6.6293	4.8089
0.3601	22.901	10.555	8.4331	8.6075	9.5682	9.9685	8.3338
0.3541	24.307	14.357	12.705	12.679	12.57	13.135	11.748
0.3482	25.644	17.449	16.081	15.983	15.351	15.932	14.931
0.3422	26.741	19.782	18.561	18.438	17.593	18.101	17.472
0.3363	27.54	21.25	20.093	19.943	18.996	19.482	19.024
0.3304	27.803	21.793	20.622	20.441	19.502	19.966	19.58
0.3244	27.557	21.44	20.162	19.961	19.219	19.675	19.316
0.3185	26.956	20.177	18.8	18.585	18.156	18.65	18.211
0.3125	26.029	18.217	16.657	16.435	16.331	16.901	16.296
0.3066	24.737	15.501	13.847	13.651	13.966	14.57	13.88
0.3007	23.438	12.296	10.471	10.347	11.29	11.868	11.263
0.2947	19.252	7.7884	6.3976	6.5034	8.4323	8.7649	8.1014
0.2888	4.9779	3.1358	3.6779	3.9093	5.9632	6.1114	5.6377
0.2829	1.9164	2.2044	2.6472	2.7974	4.3795	4.5182	4.5517
0.2769	1.4285	2.0251	2.3037	2.3593	3.5018	3.6332	4.0953
0.2710	1.4348	2.034	2.2221	2.2169	3.0498	3.203	3.9347
0.2650	1.5844	2.1088	2.2522	2.2162	2.8329	3.0335	3.9127
0.2591	1.7186	2.203	2.3336	2.2854	2.7497	3.0079	3.9426
0.2532	1.8322	2.2906	2.4247	2.3764	2.7437	3.0512	3.9667
0.2472	1.9143	2.3396	2.4741	2.4312	2.7504	3.0843	3.9316

Table C-3: Turbulent kinetic energy at r/T = 0.185

r/T = 0.185 Turbulent kinetic energy (m^2/s^{-2})							
z/H	**Upwind**	**Upwind**	**Upwind**	**Upwind**	**Central**	**QUICK**	**RNG**
	GRID 1	GRID 2	GRID3	GRID 4	GRID 4	GRID 4	GRID 4
0.4194	1.6138	2.5109	3.3488	3.8723	5.17334	5.27216	3.5015
0.4135	1.7528	2.7312	3.6312	4.1555	5.53636	5.59596	3.6286
0.4076	1.9223	3.0218	4.0413	4.6054	6.1581	6.17629	3.8255
0.4016	2.1276	3.4149	4.6061	5.2549	7.11683	7.09408	4.0955
0.3957	2.3894	3.9385	5.3867	6.179	8.5553	8.49521	4.4727
0.3898	2.8763	4.6682	6.4957	7.5239	10.7449	10.6601	5.0132
0.3838	4.0503	5.7593	8.1643	9.6066	14.2485	14.187	5.8002
0.3779	6.2201	7.7646	11.218	13.363	20.4021	20.5887	6.9779
0.3719	11.36	13.23	18.672	22.069	32.1833	33.4724	8.8478
0.3660	17.732	24.347	35.603	41.988	51.9454	55.4816	11.984
0.3601	23.952	36.125	54.052	64.977	69.1504	73.5062	15.301
0.3541	28.497	43.819	63.155	75.855	78.1882	81.0585	17.309
0.3482	29.446	44.98	63.553	75.568	77.9987	80.0925	17.605
0.3422	27.912	40.83	57.134	67.989	71.5827	73.5686	16.543
0.3363	24.648	33.978	48.486	58.686	64.2283	66.4581	15.48
0.3304	22.377	29.725	43.615	54.286	60.834	63.4121	15.773
0.3244	23.861	32.608	46.929	58.721	64.6238	67.3048	17.879
0.3185	26.35	38.195	53.615	67.068	73.0067	75.371	20.322
0.3125	28.556	41.219	57.827	72.903	80.3423	82.1591	21.394
0.3066	26.826	39.134	56.502	72.453	81.8878	83.3655	20.537
0.3007	23.424	33.144	49.481	64.05	75.3711	77.2863	18.345
0.2947	18.577	24.587	37.888	47.711	62.0612	64.8016	15.446
0.2888	12.384	15.314	22.687	27.842	43.0127	44.4917	11.595
0.2829	7.823	8.8227	13.073	16.213	27.6287	27.739	8.7365
0.2769	4.69	6.0317	8.8733	10.99	18.9456	18.6146	7.041
0.2710	2.9885	4.6543	6.7349	8.2327	13.9549	13.6136	5.9859
0.2650	2.4917	3.8527	5.4263	6.5835	10.8358	10.5877	5.2702
0.2591	2.1843	3.3191	4.6116	5.572	8.80631	8.67656	4.7456
0.2532	1.9914	2.999	4.099	4.9439	7.48181	7.45958	4.3427
0.2472	1.8613	2.7734	3.7463	4.5198	6.63847	6.68687	4.0461

Table C-4: Radial Velocity at r/T = 0.285

	r/T = 0.285 Radial Velocity (m/s)							
z/H	Upwind	Upwind	Upwind	Upwind	Central	QUICK	RNG	SM
	GRID 1	GRID 2	GRID3	GRID 4	GRID 4	GRID 4	GRID 4	GRID 4
0.4194	1.0853	1.7871	1.9723	2.0108	2.9426	2.8775	3.2152	1.4245
0.4135	1.1479	1.8493	2.0267	2.0563	3.0316	2.9527	3.2984	1.5299
0.4076	1.2198	1.9119	2.0882	2.1173	3.1186	3.0399	3.3702	1.6630
0.4016	1.3063	1.9859	2.1684	2.2037	3.2234	3.1575	3.4666	1.8733
0.3957	1.4230	2.0849	2.2891	2.3403	3.3871	3.3425	3.5935	2.2759
0.3898	1.6428	2.2524	2.5127	2.6055	3.7212	3.7021	3.7426	3.0477
0.3838	2.0305	2.6018	3.0027	3.1967	4.4659	4.4883	3.9023	4.3036
0.3779	2.6355	3.3304	4.0357	4.3676	5.8675	5.9709	4.0711	6.0285
0.3719	3.7651	4.7120	5.7350	6.1991	7.9374	8.1418	4.3085	8.1370
0.3660	5.4069	6.6767	8.0426	8.6137	10.4899	10.7786	5.0941	10.5083
0.3601	7.4735	9.3889	10.8994	11.4906	13.2987	13.6456	7.8784	12.9789
0.3541	9.9814	12.5499	14.1103	14.6192	16.1299	16.5036	13.4348	15.3400
0.3482	12.8729	15.9357	17.2840	17.6060	18.6437	18.9994	22.2832	17.3255
0.3422	15.5349	18.9194	19.7896	19.8800	20.3078	20.5934	31.4183	18.6386
0.3363	17.6740	20.6100	20.8811	20.7784	20.5996	20.7889	30.1563	19.0314
0.3304	18.1255	20.2866	20.1244	19.9574	19.3900	19.4973	20.9996	18.4147
0.3244	16.8272	18.1456	17.7805	17.6870	17.0889	17.1484	12.8865	16.9036
0.3185	14.5859	14.8797	14.6169	14.6716	14.3845	14.4165	8.3359	14.7742
0.3125	11.6913	11.4691	11.3861	11.5851	11.8349	11.8592	6.6815	12.3541
0.3066	8.9317	8.4955	8.5836	8.8616	9.6981	9.7245	6.3616	9.9460
0.3007	6.5609	6.1495	6.4659	6.7413	8.0351	8.0798	6.2522	7.7989
0.2947	4.6155	4.6678	5.1563	5.3683	6.8917	6.9773	6.0814	6.1178
0.2888	3.2805	3.8816	4.4935	4.6502	6.2165	6.3325	5.8387	5.0205
0.2829	2.5338	3.4874	4.1225	4.2502	5.7904	5.8975	5.5553	4.4063
0.2769	2.0494	3.2275	3.8428	3.9556	5.4542	5.5321	5.2712	4.0176
0.2710	1.7510	2.9968	3.5854	3.6868	5.1365	5.1863	5.0137	3.6984
0.2650	1.5437	2.7644	3.3231	3.4120	4.8083	4.8407	4.7812	3.3942
0.2591	1.3414	2.5135	3.0373	3.1104	4.4518	4.4789	4.5304	3.0887
0.2532	1.1375	2.2264	2.7161	2.7723	4.0525	4.0847	4.1855	2.7779
0.2472	0.9242	1.9166	2.3724	2.4173	3.6103	3.6578	3.7084	2.4620

Table C-5: Tangential Velocity at r/T = 0.285

r/T = 0.285 Tangential Velocity (m/s)								
z/H	**Upwind**	**Upwind**	**Upwind**	**Upwind**	**Central**	**QUICK**	**RNG**	**SM**
	GRID 1	GRID 2	GRID3	GRID 4	GRID 4	GRID 4	GRID 4	GRID 4
0.4194	0.8701	0.9667	1.0222	1.1348	1.3880	1.3487	1.4851	0.9638
0.4135	0.8385	0.9249	0.9754	1.0854	1.3150	1.2635	1.2025	0.9759
0.4076	0.8054	0.8662	0.9054	1.0130	1.2098	1.1615	0.9631	1.0108
0.4016	0.7792	0.8250	0.8550	0.9631	1.1237	1.0897	0.8338	1.0988
0.3957	0.7795	0.8174	0.8518	0.9684	1.1111	1.0930	0.7930	1.3141
0.3898	0.8536	0.8678	0.9355	1.0816	1.2701	1.2549	0.8024	1.7747
0.3838	1.0453	1.0420	1.2059	1.4237	1.7632	1.7328	0.8309	2.5481
0.3779	1.3890	1.4671	1.8361	2.1446	2.6796	2.6410	0.8635	3.6006
0.3719	2.1046	2.3361	2.9114	3.2973	3.9865	3.9757	0.9320	4.8625
0.3660	3.1732	3.6198	4.4327	4.8899	5.7537	5.8082	1.3900	6.2712
0.3601	4.5190	5.4530	6.4184	6.9204	8.0778	8.1920	3.4913	7.7526
0.3541	6.1331	7.6083	8.7239	9.2260	10.7249	10.8500	8.1805	9.1872
0.3482	7.8844	9.8544	10.9758	11.4089	13.1540	13.2452	14.7945	10.3843
0.3422	9.4228	11.7303	12.6708	12.9986	14.8046	14.8427	19.5575	11.1265
0.3363	10.6021	12.7388	13.3848	13.6031	15.3357	15.3176	19.5840	11.2445
0.3304	10.8485	12.5619	12.9154	13.0557	14.6487	14.5813	15.9607	10.6847
0.3244	10.1767	11.3000	11.3545	11.4576	12.8298	12.7279	10.3508	9.5285
0.3185	8.9560	9.2140	9.0721	9.1672	10.1739	10.0569	5.2215	7.9635
0.3125	7.3028	6.8703	6.5689	6.6698	7.2150	7.0898	2.6012	6.2154
0.3066	5.5642	4.7071	4.3436	4.4482	4.6249	4.4901	2.0077	4.4790
0.3007	4.0265	2.9950	2.7377	2.8273	2.8773	2.7670	1.9514	2.9040
0.2947	2.7417	1.9788	1.8635	1.9139	1.9813	1.9517	1.9403	1.6471
0.2888	1.8850	1.5242	1.5229	1.5373	1.6035	1.6349	1.8742	0.8631
0.2829	1.4705	1.3728	1.3981	1.3909	1.4253	1.4637	1.7455	0.5145
0.2769	1.2562	1.3215	1.3359	1.3169	1.3111	1.3311	1.5857	0.3762
0.2710	1.1861	1.3006	1.3014	1.2766	1.2293	1.2375	1.4546	0.3111
0.2650	1.1945	1.3081	1.3020	1.2773	1.1975	1.2265	1.4258	0.2740
0.2591	1.2236	1.3479	1.3560	1.3381	1.2491	1.3382	1.5566	0.2503
0.2532	1.2622	1.4282	1.4642	1.4585	1.3875	1.5615	1.8310	0.2341
0.2472	1.3008	1.5140	1.5829	1.5898	1.5396	1.7955	2.0832	0.2221

Table C-6: Turbulent kinetic energy at r/T = 0.285

	r/T = 0.285 Turbulent kinetic energy (m^2/s^{-2})							
z/H	**Upwind**	**Upwind**	**Upwind**	**Upwind**	**Central**	**QUICK**	**RNG**	**SM**
	GRID 1	GRID 2	GRID3	GRID 4	GRID 4	GRID 4	GRID 4	GRID 4
0.4194	1.9146	3.1946	4.0209	4.5109	6.5430	6.2971	4.2612	6.2205
0.4135	1.9374	3.2211	4.0803	4.5842	6.7417	6.3754	4.2680	6.6718
0.4076	1.9817	3.2559	4.1638	4.6962	7.0617	6.5404	4.2489	7.4608
0.4016	2.0747	3.3490	4.3456	4.9392	7.6602	6.9242	4.2578	9.0857
0.3957	2.2879	3.5711	4.7796	5.5212	8.9425	7.8679	4.3057	12.7746
0.3898	3.0132	4.1787	5.9234	7.0734	11.9856	10.3708	4.3812	20.3543
0.3838	4.6811	5.9349	9.0561	11.2361	18.7618	16.6057	4.4815	32.4949
0.3779	7.5892	10.2868	16.3312	19.9850	30.6664	28.5168	4.6527	47.8457
0.3719	13.5164	19.0770	28.1961	33.2589	47.3610	45.8280	5.2161	64.2216
0.3660	21.7389	31.1765	42.9776	49.1467	67.6296	66.7661	8.5338	79.4749
0.3601	31.0191	45.3972	58.2656	64.7914	88.2776	87.5719	20.2901	91.6325
0.3541	40.3075	57.6987	70.0327	76.2940	103.8957	102.8110	40.1131	99.3912
0.3482	44.9944	63.5564	74.8651	80.8929	110.9800	109.3477	55.4323	102.5878
0.3422	45.6234	62.3188	73.1691	79.7633	111.2772	109.4270	40.7754	102.6523
0.3363	43.1320	58.2279	70.2382	77.7008	109.9256	108.2788	35.3101	101.5931
0.3304	41.1663	57.2275	70.0875	77.9039	109.7160	108.2728	42.1885	100.0061
0.3244	41.9297	58.3877	69.9306	77.3626	107.7875	106.0554	35.6835	96.2641
0.3185	42.0911	55.1753	63.8713	70.5430	98.8334	96.1516	20.9802	88.1410
0.3125	39.8415	45.5411	50.2691	55.9959	80.5399	76.4516	10.3903	74.9061
0.3066	31.6809	31.2267	32.9179	37.5800	56.5650	51.1015	6.7639	57.8491
0.3007	22.7224	17.5756	17.9252	21.2789	34.7436	28.8448	5.6091	39.6041
0.2947	13.9442	8.7299	9.1862	11.2853	20.8018	16.0012	5.0624	23.5956
0.2888	7.4923	4.7932	5.8784	7.2438	14.2722	10.9450	4.7040	13.2690
0.2829	4.3539	3.5721	4.8272	5.8666	11.3771	9.0021	4.4007	8.8155
0.2769	2.6942	3.2071	4.4136	5.2991	9.8165	8.0204	4.1121	7.2199
0.2710	2.0802	3.0485	4.1954	4.9948	8.7489	7.3946	3.8528	6.5670
0.2650	1.9461	2.9821	4.0758	4.8302	7.9443	7.0023	3.6748	6.2487
0.2591	1.8977	2.9743	4.0530	4.7926	7.3811	6.8417	3.6373	6.0795
0.2532	1.9014	3.0366	4.1238	4.8676	7.0695	6.8789	3.7550	5.9898
0.2472	1.9341	3.1332	4.2413	4.9891	6.9599	7.0125	3.9469	5.9476

Table C-7: Radial Velocity at r/T = 0.389

	r/T = 0.389 Radial Velocity (m/s)						
z/H	**Upwind**	**Upwind**	**Upwind**	**Upwind**	**Central**	**QUICK**	**RNG**
	GRID 1	GRID 2	GRID3	GRID 4	GRID 4	GRID 4	GRID 4
0.4194	1.6694	2.5175	2.9219	3.144	4.1472	4.11	3.6282
0.4135	1.8493	2.7337	3.1711	3.4098	4.4775	4.4384	3.7896
0.4076	2.0582	2.9793	3.4723	3.7375	4.8994	4.8637	3.9483
0.4016	2.3095	3.2938	3.8721	4.1812	5.4818	5.4614	4.1039
0.3957	2.644	3.7272	4.4465	4.8222	6.3031	6.3196	4.2583
0.3898	3.1559	4.3729	5.2779	5.7331	7.4054	7.4838	4.4179
0.3838	3.8437	5.3095	6.4065	6.933	8.7689	8.9278	4.6018
0.3779	4.7236	6.5419	7.8206	8.3859	10.33	10.576	4.8805
0.3719	5.8946	8.071	9.4515	10.025	12.001	12.33	5.5411
0.3660	7.2775	9.7713	11.209	11.76	13.68	14.079	7.2408
0.3601	8.7963	11.64	13	13.474	15.245	15.688	10.312
0.3541	10.405	13.459	14.645	15.004	16.56	17.014	14.491
0.3482	11.936	15.018	15.96	16.18	17.494	17.925	19.202
0.3422	13.19	16.106	16.73	16.836	17.939	18.314	23.184
0.3363	14.071	16.488	16.823	16.858	17.838	18.134	24.443
0.3304	14.156	16.059	16.211	16.234	17.206	17.405	22.174
0.3244	13.498	14.945	15.001	15.061	16.118	16.214	18.107
0.3185	12.38	13.303	13.386	13.517	14.706	14.697	13.939
0.3125	10.888	11.449	11.591	11.796	13.123	13.017	10.772
0.3066	9.2415	9.5922	9.8176	10.083	11.531	11.354	9.0807
0.3007	7.6759	7.8944	8.2313	8.5304	10.076	9.8809	8.2689
0.2947	6.2256	6.5113	6.9532	7.2536	8.8618	8.7101	7.723
0.2888	4.9926	5.4932	6.0427	6.3205	7.9329	7.8619	7.259
0.2829	4.0945	4.8236	5.4308	5.6736	7.2274	7.2331	6.829
0.2769	3.4011	4.385	5.0014	5.2112	6.6681	6.7266	6.4236
0.2710	2.8896	4.055	4.6616	4.8429	6.1883	6.2785	6.0365
0.2650	2.5576	3.7778	4.3595	4.5178	5.7486	5.8565	5.6624
0.2591	2.2821	3.5178	4.0728	4.2111	5.3286	5.4452	5.2964
0.2532	2.0408	3.2641	3.7904	3.9101	4.9187	5.0374	4.9355
0.2472	1.8182	3.0094	3.5065	3.6083	4.5145	4.6306	4.5786

Table C-8: Tangential Velocity at r/T = 0.389

r/T = 0.389 Tangential Velocity (m/s)							
z/H	**Upwind**	**Upwind**	**Upwind**	**Upwind**	**Central**	**QUICK**	**RNG**
	GRID 1	GRID 2	GRID3	GRID 4	GRID 4	GRID 4	GRID 4
0.4194	0.9041	0.8892	0.9162	1.0235	1.3084	1.2681	1.3637
0.4135	0.9174	0.9047	0.9411	1.0562	1.3501	1.3054	1.3408
0.4076	0.9426	0.9332	0.9885	1.1161	1.4292	1.3797	1.3145
0.4016	0.9862	0.9912	1.0797	1.2284	1.5769	1.5247	1.2844
0.3957	1.0667	1.1018	1.2518	1.4335	1.8321	1.784	1.2509
0.3898	1.2308	1.3114	1.5491	1.7713	2.221	2.1876	1.2154
0.3838	1.4821	1.664	1.9984	2.2568	2.7402	2.7326	1.1822
0.3779	1.8306	2.1691	2.5994	2.8756	3.3619	3.389	1.1729
0.3719	2.335	2.8332	3.32	3.5954	4.0444	4.1118	1.3096
0.3660	2.9529	3.5944	4.1153	4.3727	4.7377	4.8468	1.9618
0.3601	3.6457	4.4513	4.9384	5.1485	5.3825	5.529	3.4159
0.3541	4.3915	5.2956	5.7002	5.8427	5.9136	6.0864	5.5566
0.3482	5.1064	6.025	6.3068	6.369	6.2657	6.4468	8.0197
0.3422	5.6931	6.5325	6.6476	6.6414	6.3845	6.5512	10.103
0.3363	6.1055	6.6998	6.6513	6.5998	6.2432	6.3735	10.768
0.3304	6.1478	6.4718	6.302	6.2371	5.8539	5.9303	9.5049
0.3244	5.8418	5.9053	5.6541	5.6059	5.2634	5.2776	7.0638
0.3185	5.3173	5.0775	4.8119	4.8018	4.5454	4.4997	4.3895
0.3125	4.6118	4.1481	3.8962	3.9324	3.7806	3.6884	2.361
0.3066	3.8272	3.2297	3.0189	3.097	3.0476	2.9332	1.4407
0.3007	3.0849	2.4093	2.2691	2.3763	2.412	2.3095	1.1403
0.2947	2.4046	1.774	1.7062	1.8246	1.9141	1.8566	0.9976
0.2888	1.8442	1.343	1.347	1.4629	1.565	1.5646	0.8914
0.2829	1.4634	1.0981	1.1425	1.2489	1.3272	1.3747	0.7963
0.2769	1.1919	0.9709	1.0267	1.1238	1.16	1.2383	0.7074
0.2710	1.0174	0.8968	0.9523	1.0419	1.0312	1.1268	0.6229
0.2650	0.9355	0.8488	0.8957	0.9801	0.9235	1.0278	0.5427
0.2591	0.8834	0.8109	0.8481	0.9286	0.8287	0.9367	0.469
0.2532	0.8505	0.7805	0.8066	0.8835	0.7437	0.8525	0.4051
0.2472	0.83	0.7549	0.7705	0.8437	0.6673	0.7756	0.3535

Table C-9: Turbulent kinetic energy at r/T = 0.389

r/T = 0.389 Turbulent kinetic energy (m^2/s^{-2})							
z/H	**Upwind**	**Upwind**	**Upwind**	**Upwind**	**Central**	**QUICK**	**RNG**
	GRID 1	GRID 2	GRID3	GRID 4	GRID 4	GRID 4	GRID 4
0.4194	2.8444	4.2823	5.3868	6.0061	8.23849	8.25053	3.8785
0.4135	2.8942	4.3709	5.6213	6.3379	8.90284	8.89373	3.8889
0.4076	3.0629	4.608	6.1445	7.0379	10.1766	10.1599	3.8973
0.4016	3.4108	5.1876	7.2251	8.4382	12.4965	12.5205	3.9026
0.3957	4.1155	6.3784	9.3118	11.032	16.3099	16.4713	3.9081
0.3898	5.618	8.6892	12.859	15.189	21.6975	22.0981	3.9287
0.3838	7.9054	12.499	17.924	20.758	28.1732	28.8477	4.023
0.3779	11.028	17.618	23.998	27.061	34.8903	35.7787	4.4643
0.3719	15.18	23.519	30.148	33.184	40.9456	41.9154	6.5413
0.3660	19.599	29.195	35.418	38.233	45.6032	46.4963	13.146
0.3601	23.811	33.713	39.083	41.507	48.4997	49.1853	24.167
0.3541	27.251	36.396	40.689	42.824	49.7506	50.1645	34.966
0.3482	28.655	36.861	40.521	42.598	49.79	49.9304	39.823
0.3422	28.904	36.003	39.429	41.626	49.1266	49.014	36.626
0.3363	28.306	34.951	38.331	40.598	48.0296	47.6477	32.924
0.3304	27.76	34.319	37.377	39.565	46.3514	45.6117	34.163
0.3244	27.534	33.568	35.887	37.908	43.6601	42.4274	32.112
0.3185	26.923	31.479	32.988	34.879	39.5726	37.7322	22.989
0.3125	25.509	27.661	28.338	30.193	34.0691	31.6071	11.892
0.3066	22.069	22.093	22.369	24.268	27.6752	24.7678	5.9458
0.3007	17.97	16.003	16.202	18.089	21.3482	18.3994	4.3123
0.2947	13.533	10.602	10.99	12.743	16.0187	13.53	3.8488
0.2888	9.3595	6.7695	7.5538	9.0362	12.2579	10.4977	3.6102
0.2829	6.4264	4.6561	5.6991	6.9082	9.91646	8.81925	3.4204
0.2769	4.343	3.6863	4.7969	5.8098	8.54403	7.90905	3.2462
0.2710	3.0521	3.2328	4.3542	5.2354	7.72556	7.3871	3.0807
0.2650	2.5323	3.032	4.1142	4.9165	7.21432	7.06684	2.9226
0.2591	2.2519	2.9268	3.9783	4.7328	6.88396	6.86231	2.7726
0.2532	2.1234	2.8858	3.9052	4.6315	6.67205	6.73448	2.6336
0.2472	2.0914	2.8788	3.8769	4.5878	6.54616	6.66555	2.5103